UCLA
UCLA Electronic Theses and Dissertations

Title
Thermodynamic Screening of Reaction Chemistries for Atomic Layer Etching of Metals

Permalink
https://escholarship.org/uc/item/8p6071qm

Author
Xia, Yantao

Publication Date
2020

Peer reviewed|Thesis/dissertation

eScholarship.org Powered by the California Digital Library
University of California

UNIVERSITY OF CALIFORNIA

Los Angeles

Thermodynamic Screening of Reaction Chemistries for Atomic Layer Etching of Metals

A thesis submitted in partial satisfaction

of the requirements for the degree

Master of Science in Chemical Engineering

by

Yantao Xia

2020

© Copyright by

Yantao Xia

2020

ABSTRACT OF THE THESIS

Thermodynamic Screening of Reaction Chemistries for Atomic Layer Etching of Metals

by

Yantao Xia
Master of Science in Chemical Engineering
University of California, Los Angeles, 2020
Professor Philippe Sautet, Chair

A framework to study the thermodynamics of chemistries of the etching step in ALE processes is presented. The effects of two modifiers(O & N), two substrates(Cu & Ni) and two etchants(formic acid and formamidine) on etching energy are studied with two models. The bulk model uses the bulk formation energy to provide a quick estimate of the etching energy, while the layer model incorporates effects of surface stability and adsorbate configurations. The effect of etchants is independent of models used. Etching by formic acid is favored by 0.45 eV on Ni but slightly disfavored by 0.07 eV on Cu. The two models produce the same qualitative results: on the bare metal, all modifier/etchant pair is unfavorable; on activated substrates, etching is unfavorable for Ni but favorable for Cu. The bulk model shows that the effect of modifiers is insignificant on Cu, but on Ni the O activation is favored by 0.20 eV. With the layer model, a difference of $\sim$ 0.3 eV favoring the N activation is observed for Cu substrate. On Ni substrate this effect depends on coverage. Below $\sim 0.07\text{Å}^{-2}$, N is the favored modifier. The reverse is true above $\sim 0.07\text{Å}^{-2}$. The layer model is applied to metastable structures on Ni/O/FAmd system formed by placing O atoms in sublayer interstitial sites, resulting in a favorable etching energy consistent with the experiments. The validity of the layer model is established, but the structures fed into the model must be carefully selected to match with the actual substrate.

The thesis of Yantao Xia is approved.

Jane Pei-Chen Chang

Daniel Neuhauser

Philippe Sautet, Committee Chair

University of California, Los Angeles

2020

Contents

List of Figures . . . . **vi**

List of Tables . . . . **vii**

Preface . . . . **viii**

1 Introduction **1**

2 Methods **9**

2.1 The plasma and thermodynamic equilibria 9

2.2 Computational methods 10

2.3 Bulk lattice and molecular structure determination 11

3 The bulk model **16**

4 Layer model **24**

4.1 Derivation of etching energy expression 24

4.2 Substrate definitions and adsorption site identification 27

4.3 Adsorption configuration search 33

4.4 Etching energies by termination 38

4.5 Determination of chemical potential and phase distribution 40

4.6 Average etching energies 44

5 Ni/O/HFA process and metastable structures **47**

6 Summary and Conclusion **52**

A Computational details **55**

B Structural parameters of the metal complexes **56**

C Configuration search iterations **57**

Bibliography **70**

List of Figures

1.1 Etching profiles of continuous dry etching techniques 2

1.2 $Si/Cl_2/Ar$ plasma ALE Process 4

1.3 Al_2O_3/HF/TMA thermal ALE process 5

2.1 Energetics of plasma-enhanced chemistry 9

2.2 Molecular structures and electronic energies of complexes and etchants 15

4.1 Path for evaluating layer model etching energy 25

4.2 Overlayer adsorption sites used in configuration search 31

4.3 Adsorption energies of overlayer structures by termination 36

4.4 Etching energies of overlayer structures by termination 39

4.5 Correspondance of modifier coverage to chemical potential 42

4.6 Surface energies of overlayer structures by termination at varying chemical potential 43

4.7 Average etching energies from the layer model 45

5.1 Relaxaed overlayer, mixed, and sublayer structures 49

5.2 Etching energies of Ni/O system at overlayer, mixed, and sublayer structures. . 51

C.1 Configuration search iterations for Ni/N system 60

C.2 Configuration search iterations for Cu/N system 63

C.3 Configuration search iterations for Ni/O system 66

C.4 Configuration search iterations for Cu/O system 69

List of Tables

2.1 Optimized bulk lattice and formation energy 12

3.1 $\Delta G_{\mathrm{et,M}}$, etching energy on pristine substrates from the bulk model 19

3.2 $\Delta G_{\mathrm{et,MX}}$, etching energy on activated substrates from the bulk model 20

3.3 $\Delta G_{\mathrm{et,M}} - \Delta G_{\mathrm{et,MX}}$, etching energies difference of pristine and activated substrates 20

3.4 Energy decomposition of bulk model 23

4.1 Definitions of substrate supercells and layers 28

4.2 Initial adsorption energies of overlayer sites and name-label correspondence . . . 29

4.3 Experimental surface oxide structures 34

5.1 Adsorption energies of sublayer sites 49

B.1 Structural parameters of the organometallic complexes 56

Preface

The author gratefully acknowledges the support from UCLA Institute of Digital Research and Education(IDRE) for computational resources on the UCLA Hoffman2 cluster.

This work used the the Extreme Science and Engineering Discovery Environment(XSEDE) Comet cluster at San Diego Supercomputer Center through allocation TG-CHE170060. XSEDE is supported by National Science Foundation Grant number ACI-1548562.

Results from "Xia Sang, Yantao Xia, Philippe Sautet, and Jane P. Chang. Atomic layer etching of metals with anisotropy, specificity, and selectivity. Journal of Vacuum Science and Technology A, (2020, Accepted)" is reproduced Chapter 5.

CHAPTER 1

Introduction

The spectacular growth of information technology is to a large extent fueled by the ever-succeeding attempt of the semiconductor industry at feature size scaling. The urgency of this eventual goal increases as single-digit nanometer technology nodes are approached. The introduction of 3D devices makes it necessary to control vertical film thickness, in addition to the already stringent requirement of patterning planar features. At the same time, significant advances are possible with introduction of new materials to the circuitry. As the introduction of extreme ultraviolet photolithography suffers from repeated delays, the burden of keeping up with Moore's law increasingly falls on developing more precise etching processes. To achieve the required device fidelity on hard-to-etch metals with complex geometries, a general approach to engineering metal surfaces on the atomic scale is urgently needed[8].

The focus of the present thesis is etching metals. Conventional wet etching approaches used in the fields of metallurgy and art exposes patterned metals to various acids. Metal becomes oxidized and dissolve into the liquid phase. Wet etching offers fast etch speed but the Brownian motion of the etchant molecules always results in uniform etching in all directions(isotropic etching), rendering it unsuitable to pattern the high aspect ratios structures today. In addition, the harsh chemical conditions may be corrosive to existing structures.

Today, dry etching is the dominant technique for patterning. Two mechanism are at work in dry etching: (1) chemical etch process, in which neutral radicals react with the surface, producing volatile products, and (2) sputtering, which relies on the kinetic energy of inert ions to disrupt the lattice and eject substrate atoms. Common etching techniques are shown in Figure 1.1. Neutral chemical etch (**A**) is always isotropic, able to reach underneath

masking material. In sputtering(**B**), the ions are accelerated toward the substrate, leading to vertical direction being preferred, but the side wall slopes outward due to the finite mean free paths of the ions, making it difficult to create high-aspect ratio structures. In reactive ion etching(RIE, **C**), nearly vertical side wall is achieved when chemical etch is re-introduced. In this technique, mechanisms (1) and (2) cooperate. Structures with still higher aspect ratios are possible with inhibitor films in ion-enhanced inhibitor etching(**D**), where the sidewalls are protected from etchant contamination by repeated deposition of the inhibitor.

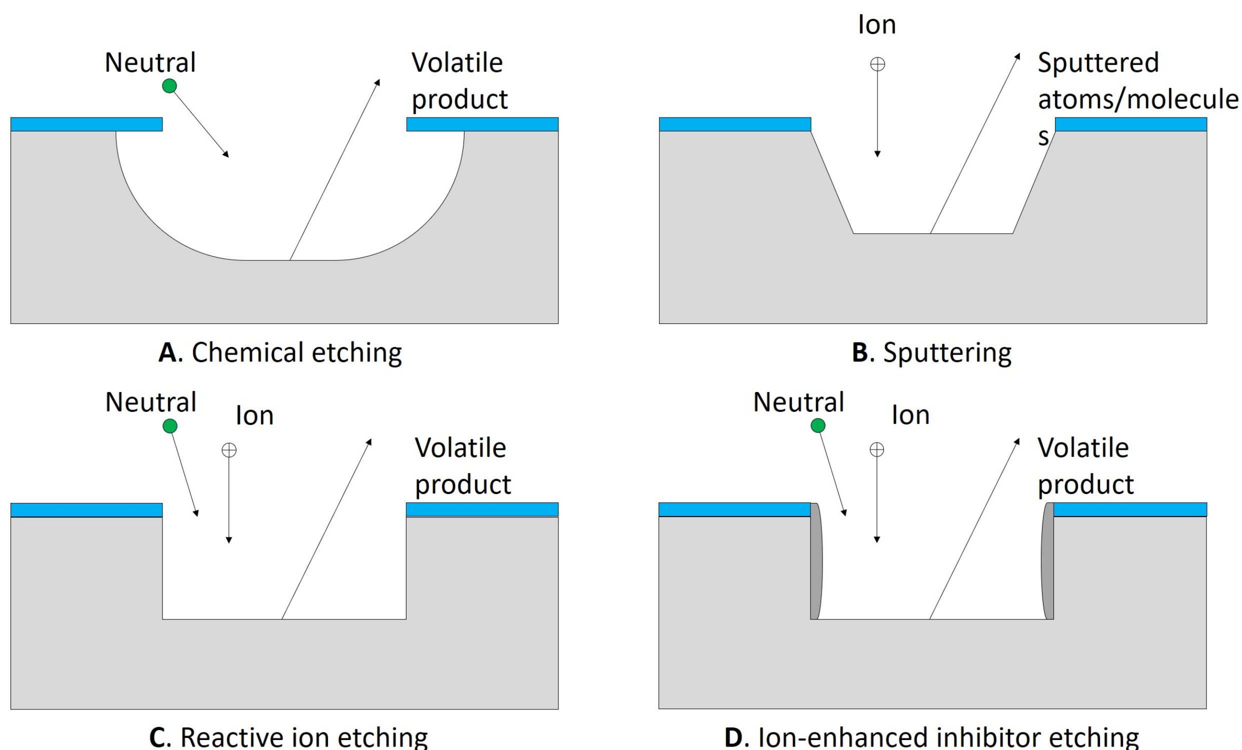

Figure 1.1: Schematic of different vertical etching profiles. **A)** neutral radicals in chemical etching produce isotropic profiles. The substrate underneath the mask is etched away. **B)** sputtering is anisotropic, but cannot create deep trenches due to the non-vertical sidewall. **C)** Ion-enhanced etching is able to create near-vertical sidewalls. **D)** Inhibitor etching protects the sidewall by an inhibitor, enabling even higher aspect ratio and prevents excessive sidewall damage from neutrals(reactive radicals).

A major drawback of the aforementioned existing continuous dry etching techniques is

their inability to precisely control vertical etch thickness, which provides the opportunity window for atomic layer etching(ALE).

The conceptual reverse of atomic layer deposition(ALD), ALE was first reported in the 1980s. While ALD has since saw wide-range industry adoption, ALE was considered too slow to be practical until developments in the last decade brought it back under intense investigation when applications emerged where precision rather than speed is the bottleneck[21]. The technique can be thought of as RIE with time separated doses. In RIE, ions and radicals are present in the same time frame. In ALE, the ions and radicals are introduced in time-separated pulses. The ions are used to modify the surface, creating a surface layer of different chemical composition, but do not themselves sputter etch. The neutrals are introduced after ions are purged. The removal is accomplished either by sputtering with inert species (e.g. Ar) or reaction that forms a volatile compound. Under both scenarios, only the activated pattern is removed, and thickness reduction stops when the pristine substrate is exposed. In both steps, the reaction limits itself to the surface layers. In contrast to RIE, in ALE the energy of the ions must be kept as low as possible to avoid sputtering and/or diffusion deep inside the substrate. The self-limiting nature of the reaction enables precise thickness control, since the etch rate no longer depends on exposure time.

The main engineering challenge in ALE is that surface reactions must be mutually exclusive. Consider the plasma ALE process on Si[47], depicted in Figure 1.2. In the activation step, plasma-assisted chlorine adsorption activates the Si surface. The energy source for removal step is Ar^+ plasma. In the activation step, the ion energies must be kept low to stay in the ALE regime. In this case, the process window that allows for ALE is 40-60V in terms of RF bias in the chlorination step. Higher energies result in a loss of selectivity to the sputtering mechanism. Etching at lower energies are too slow. At the middle of this range, etch-per-cycle(EPC) is ~ 12Å, corresponding to roughly 3 layers of atoms.

The fact that the same chemistry can be used in both ALE and continuous modes enables an interesting comparison. If Cl_2 and Ar doses are not time separated, a continuous etch results. Within the ALE bias voltage window, the selectivity of ALE is an order of magnitude higher than that of RIE.

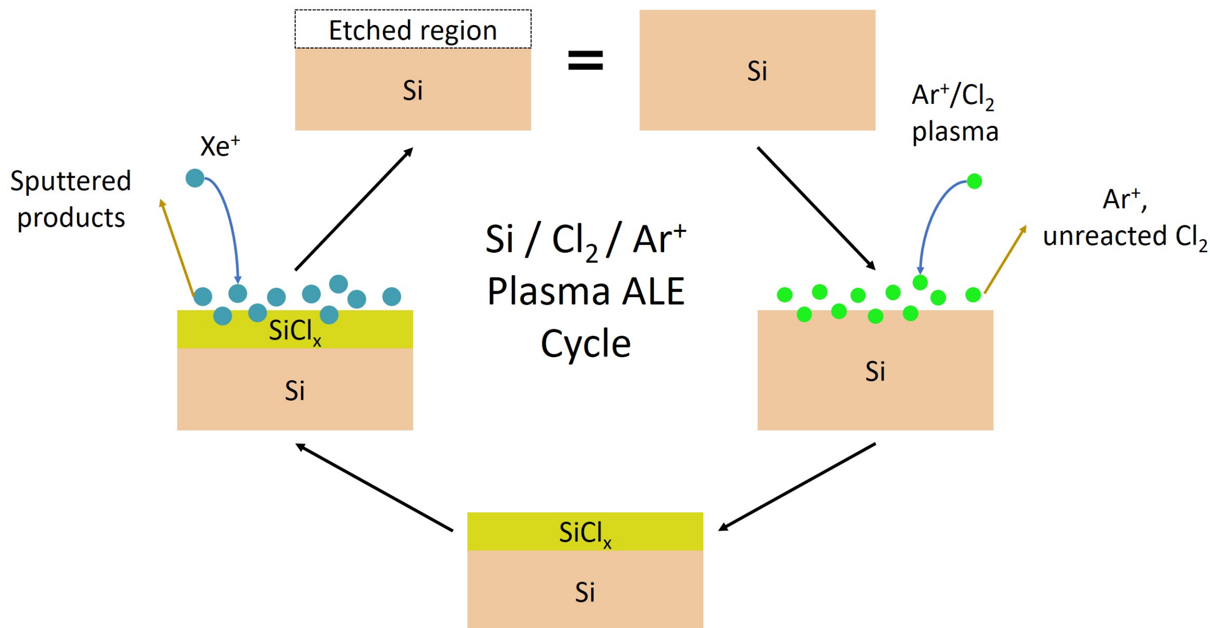

Figure 1.2: $Si/Cl_2/Ar$ plasma ALE Process. Chlorination-activated Si surface is sputter-etched with Ar^+ plasma.

Here, the chlorine activation must be self-limiting, because if Cl atoms migrates indefinitely into the Si layer the thickness of $SiCl_4$-like layer formed(and subsequently etched) would be dependent on Ar^+ exposure time. Similarly, Ar^+ plasma must not be energetic enough to sputter the Si substrate on its own.

The $Si/Cl_2/Ar^+$ example is entirely plasma based. The alternative, thermal ALE, is discussed in the next example. Consider the process depicted in Figure 1.3. HF gas adsorbs on the surface of alumina(Al_2O_3) to form a stable and nonvolatile AlF_3-like layer, releasing H_2O as a by-product. After purging HF, the AlF_3 layer is reacted with trimethylaluminum(TMA) to form the volatile $AlF(CH_3)_2$ complex that must be purged before the HF is re-introduced. The dangling methyl groups on the surface are removed at the next cycle by HF to form methane. In addition to the same requirement that fluorination does not proceed indefinitely, and that TMA is not reactive on Al_2O_3, the case here is complicated by the fact that TMA and HF are used for ALD of AlF_3 at lower temperatures. The ALE reaction can be

written in overall(unbalanced) as follows:

$$AlF_3 + Al_2O_3 + Al(CH_3)_3 \longrightarrow AlF(CH_3)_2\uparrow + AlO_x(CH_3)_{3-x} \quad \{1.1a\}$$

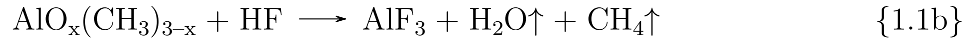

$$AlO_x(CH_3)_{3-x} + HF \longrightarrow AlF_3 + H_2O\uparrow + CH_4\uparrow \quad \{1.1b\}$$

The competing ALD reaction is as follows:

$$AlF_3{-}HF + Al(CH_3)_3 \longrightarrow AlF_x(CH_3)_{3-x}\downarrow + CH_4\uparrow \quad \{1.2a\}$$

$$AlF_x(CH_3)_{3-x} + HF \longrightarrow AlF_3{-}HF + CH_4\uparrow \quad \{1.2b\}$$

The competition between ALE of Al_2O_3 and ALD of AlF_3 makes the time separation of doses critical, as the simultaneous presence of HF and the etching product $Al(acac)_3$ leads to deposition of AlF_3.

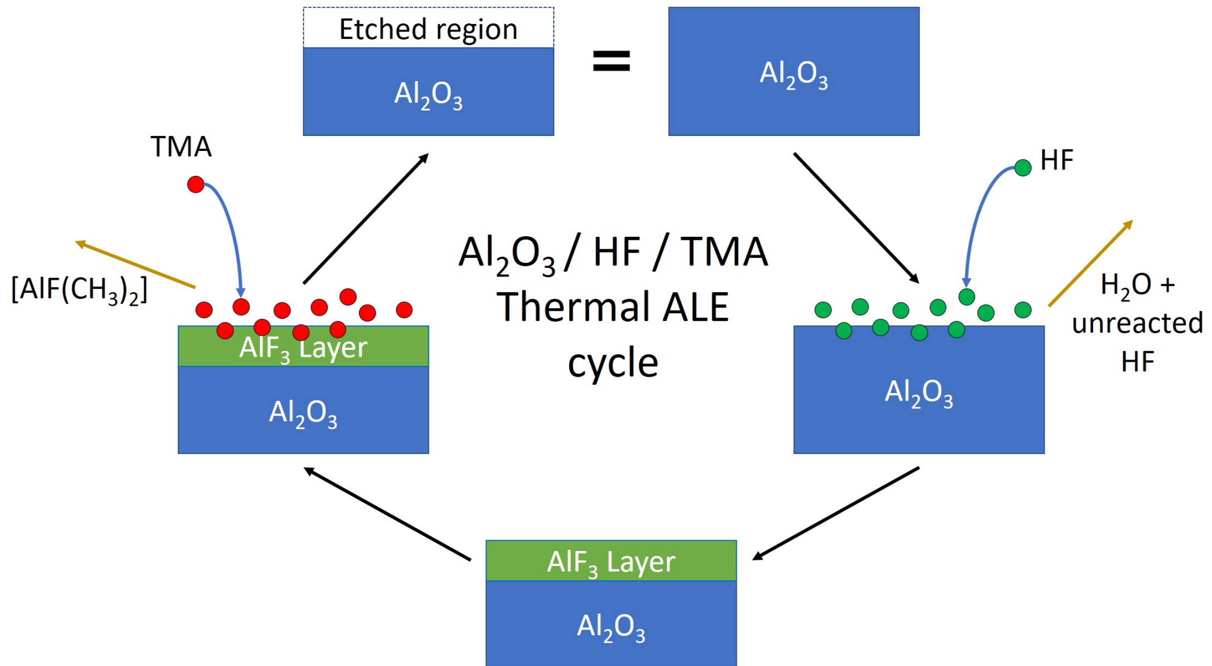

Figure 1.3: Al_2O_3 thermal ALE Process. Fluorine-activated Al_2O_3 is etched with tetramethylaluminum(TMA).

The defining feature of ALE is not the exact removal of one layer of atoms, but rather the well-defined etch thickness(etch-per-cycle, EPC), independent of the exposure time. The amount of material removal can be controlled easily via the number of cycles. From a

practical point of view, it is difficult to determine exactly the number of atomic layers removed. In this sense, demanding the strict "atomic-layer" level of control is not meaningful at the present.

Both steps have the choice of being a thermal or plasma process. Plasma works to facilitate the reaction thermodynamically by increasing overall reaction free energy gain, and kinetically by lowering activation energy barrier, respectively. For the activation step, some substrates/modifier combinations(termed "system" subsequently) are simply non-reactive under thermal conditions(e.g. Cu with N_2). More importantly, plasma is required in either activation or etching for the whole process to be anisotropic. On the other hand, the energetic species in even low-energy plasmas(with ion energies of 10-20 eV) can damage the existing structure, leading to device failure. The ideal plasma ALE process would use a low-energy plasma such the only effect of modifier ions is directional activation, devoid of any sputtering[1, 22].

Metallic systems play a key role in logic gates and interconnects[32]. Traditional continuous metal etching is plagued by the re-deposition problem since the metal vapor has a strong driving force to recombine. The problem can be circumvented if the metal atoms in the vapor is stabilized by organic ligands to form stable, volatile metal complexes. This in turn requires a thermal etching step. The activation step must then be plasma-assisted. Plasma can also act as energy source in the activation step, as in the Si plasma ALE example. Extra source of energy is especially important on the noble metals(e.g. Cu). These fundamental considerations suggest that a thermal/plasma mixed process is ideal for metal ALE.

At the turn of the century, first principles modeling on extended surface was prohibitively expensive. Practical constraints led researchers to use empirical force fields[2, 44]. It has since become clear that successful discovery of ALE requires a deeper understanding of self-limiting surface reactions, for which empirical force fields are insufficient. Recent advances in ab-initio computational chemistry methods(particularly density functional theory(DFT)) and the explosion in computational power have made simulations of large-scale surface processes possible.

Existing computational investigations offer little guidance on process discovery. Rather, studies follows the pattern of microkinetic studies in the computational catalysis field[15]. When the precursors/etchants are not known precisely, such detailed knowledge is not warranted. Since the number of demonstrated ALE processes is still very limited, *in silico* ALE process discovery, if possible, can provide great impetus to the field. The first step toward this goal is the accurate evaluation of the thermodynamics involved.

The metals of widest industrial interest are Cu, Ni, Fe, Zn, and Co[35], of which Cu and Ni are the concerns of this study. Cu is by far the most-used metal in circuitry, mainly as interconnects. As features scale down, Ni interconnects have the potential to replace the Cu counterpart, due to its decreased electron mean free path. Other applications of Ni include EUV photolithography masks and optical storage material.

Oxygen and nitrogen are selected as modifiers. Oxygen is the most used modifier in ALE/ALD after the halogens, but using O as the modifier is problematic because the presence of native oxides on surfaces can create unintended activation. Nitrogen were selected to explore the possibility of replacing oxide based processes. Although existing ALE processes often use halogen-activated surfaces, it is desirable to avoid them, for their high reactivity leads to side wall damage.

For etchants, formic acid(HFA) and formamidine(HFAmd) were selected as representatives of the carboxylato- and amidinato- families of compounds, both of which have had successes in ALE/ALD of transition metals[31, 28, 32, 45]. The two families provide many opportunities for functionalization, making them highly versatile for etchant design. The systematic study of etchant is not the focus of this study, hence the amidinate and carboxylate structures are limited to non-substituted formamidine and formic acid ligands, respectively.

At the time of writing, a working process based on oxygen plasma activated Ni with HFA as the etching chemistry has been demonstrated[45]. Considered the target process, Gibbs free energies and chemical potential used to calculate adsorption energies are evaluated at the demonstrated conditions(80°C and 350 Torr).

The thesis is organized as follows. In Chapter 1, a brief survey of etching techniques

is given, highlighting the need for new metal etching processes, ALE's unique position to fulfill that need, and the role of simulations. In Chapter 2 discusses elements of methods applicable to all subsequent models, including a brief description of plasma physics, DFT, and details on the determination of complex structures. Chapter 3 discusses the methods and results specific to the bulk model. Chapter 4 derives the layer model with the Ni/O example, with applications to proposed ALE processes with substrates/modifiers/etchants discussed above. Chapter 5 probes the metastable structures formed due to lattice disruption by ions in plasma activation step. Conclusions and future directions are discussed in Chapter 6.

CHAPTER 2

Methods

2.1 The plasma and thermodynamic equilibria

Plasma is formed when the electrons in gas phase atoms/molecules are excited. The molecules can dissociate, ionize, creating a sea of energetic free electrons and excited species. The working principle of plasma-assisted reactions is illustrated in Figure 2.1. By increasing the energy of the reactant, activation energy E_a is decreased, and a normally endothermic reaction can be made exothermic since the final product on the surface is not excited. Energy is still conserved because continuous energy input is required to sustain the plasma as excited states spontaneously decay to the ground state, releasing energy in the form of light and heat.

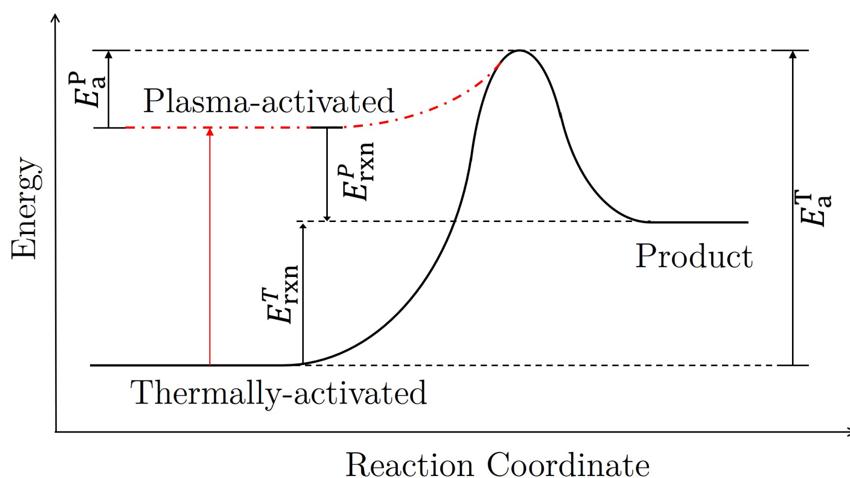

Figure 2.1: Energetics of plasma-enhanced chemistry. A thermal reaction with a positive E_rxn^T (endothermic) is converted to a plasma reaction with a negative E_rxn^P. The large kinetic barrier E_a^T is also decreased to E_a^P in the plasma process, resulting in a much higher reaction rate.

While the energy can be supplied in thermally by heating gases to high temperatures(e.g. a flame), thermal plasma cannot be used for semiconductor fabrication. At the temperatures processes can operate at, thermal energy alone is not enough to ionize the gases appreciably. Since the target is to ionize, not to accelerate, electric fields can selectively transfer energy to the ions and electrons. A DC plasma is formed when a strong DC field is applied across a gas. Electrons and ions are accelerated toward the cathode, and cathode, respectively. If the acceleration is greater than electrostatic force holding the electrons to the nucleus, ionization results. Various other methods for plasma generation exist but they do not concern us here. It is enough to understand that a plasma is an inter-penetrating fluid of free electrons, radicals, excited states of molecules, fragments, atoms, and ions. The bulk of the plasma is charge-neutral, but a thin, negatively charged sheath is maintained at the boundary of the plasma. The sheath keeps the electrons inside the bulk plasma, but accelerates the ions toward the surface. The determination of the composition, the subject of plasma diagnostics, is difficult if not impossible[9, 10].

While plasma processing is a non-equilibrium process in the sense that electrons are not at thermal equilibrium with other species, whether the heavier species are at equilibrium is a different question. The equilibrium among the heavy species within the plasma, between the plasma and the substrate, and among the surface phases on the substrate depend on the pressure, temperature, and time scale of the process. It is natural to assume the surface-plasma reactions are equilibrated, given the self-limiting nature of ALE activation step. The equilibrium among surface phases is also assumed to allow determination of surface fractions.

2.2 Computational methods

The primary computational chemistry method used in this study is density functional theory(DFT). The Hohenberg-Kohn theorem[19] transformed the complicated many-body problem of solving the Schroedinger equation into one that solves for the electron density, which depends only on three coordinates. A unique but unknown functional on the density then yields all the properties of the system. In practical Kohn-Sham DFT implementations[23],

the unknown exact functional is approximated with an analytical inexact functional.

All quantitative results used in this thesis are obtained using Vienna Ab-initio Simulation Package(VASP)[24, 25] using the projector-augmented wave(PAW) formalism[6, 26]. The PBE[42] exchange-correlation functional is used for bulk lattice parameter optimization, surface slab models, and isolated molecular/atomic species. A progressively finer numerical setup is used in structural relaxations, but all final values listed in the main text are calculated at the same level of accuracy. In cases where molecular isomerism is difficult to resolve using PBE in VASP, the most stable structure is determined in Gaussian'16[16] + B3LYP[5, 27] functional. Gaussian is also used as a pre-optimizer for larger molecules. More details about computational setup can be found in the Appendix A.

2.3 Bulk lattice and molecular structure determination

Lattice parameters of Cu, Ni, and their oxides/nitrides are re-optimized from their experimental values to avoid any artefactual strain. The choice of bulk species is motivated by the species most likely present in the target process.

Cu_3N and Ni_3N are the only principal nitrides of copper and nickel, respectively. Other structures are claimed but are rare. Both nitrides have a positive standard Gibbs free energy of formation(meaning that they would spontaneously decompose to the metal and N_2 gas under ambient conditions), hence their synthesis typically require non-equilibrium techniques such as RF reactive sputtering[54] and DC magnetron sputtering[38]. Recently, ALD processes of Cu_3N and Ni_3N films were reported[41, 29, 50]. All of these are deposition techniques: Ni and N atoms are introduced in vapor phase and deposit on the substrate. However, a N-enabled ALE requires direct activation of metal substrate by nitrogen, for which success is reported with plasma-assisted ion implantation technique[48].

Copper oxide has three major phases: Cu_2O, CuO, and CuO_2. It is known that Cu_2O is formed when Cu(111) surface is exposed to oxygen[20]. Computational investigation suggest that similar effects would be present for at least Cu(100) and Cu(110)[12, 34]. NiO is the only known nickel oxide and its presence as a native oxide on Ni films is reported[18]. The

structures and bulk formation energies of the nitrides and oxides are summarized in Table 2.1.

Table 2.1: Optimized bulk lattice and formation energy. All experimental values are obtained from *CRC Handbook of Chemistry and Physics*[11] unless otherwise stated. The two numbers in Ni_3N lattice correspond to a and c, respectively.

	Lattice [Å]		Atomization Energy [eV]	
System	Exp.	Calc.	Exp.	Calc.
Ni	3.52	3.52	4.45	4.65
Cu	3.62	3.64	3.50	3.49
NiO	4.18	4.20	9.52[7]	8.96
Cu_2O	4.27	4.31	11.32	10.18
Ni_3N	4.64/4.31[49]	4.62/4.31	N/A	19.05
Cu_3N	3.81	3.83	14.62[14]	14.52

The optimized geometries agree very well with experiments. The lattice constants of metals and the nitrides differ less than 0.02 Å. The oxides are over-binded, as expected. The formation energies likewise agree well calorimetry data, differing no more than 0.2 eV per stoichiometric unit, the inherent inaccuracy in DFT. Experimental values are used for the oxide systems(NiO and Cu_2O) since these are well-known pathological cases for DFT. PBE functional is known to significantly underestimate the electron correlation effects and over-binds these oxides. The PBE results are kept here for completeness.

Formamidine(HFA, $HN{=}CHNH_2$)and formic acid(HFAmd, HCOOH) are small molecules with well-known structures but their metal complexes are either not characterized in the gas phase or experimental results conflict among themselves. For consistency, *in silico* structural determination is done for complexes used in this study wherever conclusive evidence is lacking. A note on terminology: throughout the text, HFA is used to refer to the neutral formic acid molecule, and FA refers to the ligand. The same convention is observed for the formamidine etchant and the ligand. The protonated neutral molecule are termed etchants, the deprotonated charged fragments are called ligands.

XRD on a range of copper(I) amidinates of the formula $[R'NC(R)NR''Cu]_2$ (R' and R" = *n*-propyl, isopropyl, *n*-butyl, isobutyl, *sec*-butyl, *tert*-butyl; R = methyl, *n*-butyl) in the solid phase suggest a planar dimer structure[31]. Since this is a molecular crystal, the gas phase configuration is assumed to be the same.

Nickel(II) amidinate complex was first synthesized by Gordon et. al.[32]. Distorted square planar and tetrahedron structures were proposed, but the experimental structure characterization is inconclusive. On the basis of it having similar ^{1}H nuclear magnetic resonance(NMR) data and sublimation temperature to the Co(II) equivalent, the Ni complexes were determined to have a distorted tetrahedron structure. But neither NMR nor sublimation is conclusive structural evidence. This problem was investigated in an early DFT study[28] with the PW-91 exchange-correlation functional, implemented in the DMol^3 package. The stability of the two configurations were compared for a series of complexes $Ni(RNC(R')R)_2$ where R = *i*-Pr, *t*-Bu, *s*-Bu or *t*-Bu and R'= Me, Et or trifluoroethyl. The results point to the tetrahedron being around 6 kcal/mol(0.26 eV) more stable than the square planar configuration for the formamidinate. On the other hand, it is noted that planar configurations might become more favorable if aryl groups are used for both R and R' substituents[37].

The electronic energies of planar and tetrahedral configurations of the nickel formamidinate complexes were calculated. PAW-PBE calculations show that the planar complex is 0.5 eV more stable than the tetrahedron, contradicting the literature calculations. Confirmation was sought with PAW-B3LYP, considered better for organic molecules. The result indicates that the planar configuration is favored by 0.2 eV. A Gaussian 16[16] calculation with B3LYP hybrid functional in a localized basis sets(TZV on Ni atom, 6-31G(d,p) on the rest) shows a trajectory from tetrahedron into the square planar configuration. These pieces of evidence allowed us to conclude that the square planar configuration is preferred in the gas phase.

Nickel formate crystallizes in monoclinic crystal structure with space group $P2_1/c$[53]. Information on the gas-phase molecule is lacking. Taking one stoichiometric unit of the crystal and removing the water ligands results in a monodentate structure, but it was found to be unstable by 1.5 eV compared with the bidentate structures. For the bidentate structures,

a similar problem of distorted square planar vs. tetrahedral structure is found here. The square planar configuration is found to be more stable by 0.5 eV. Since the square planar structure is typical of 16-electron Ni(II) d^8 complexes[3], higher levels of theory were not attempted.

Adsorbed formate in monodentate, bidentate, and ionic forms are present on Cu, Cu_2O, CuO surfaces[33]. Early mass spectroscopy suggests a formate dimerizes in vapor phase[13, 39]. Although no direct structural determination exists for the formate complex, the related copper acetate complex is shown to crystallize in the $P2_1/m$ space group as infinite sheets of 8-membered rings[40]. The high vapor pressure of the complex suggest there is little structural difference between the vapor and the solid phases of the copper acetate complex. Inferring from this evidence, copper(I) formate complex is taken to be a dimer structure in vapor phase.

The molecular structures can be visualized in Figure 2.2. The electronic energies used to determine relative stabilities are also listed. The reader is reminded that at the present, experimental confirmation of their existence as ALE products is lacking.

In all subsequent discussion, the Gibbs free energy G is used instead of the electronic energies. For the molecules, the translational, rotational, and vibrational contributions are considered. The correction for zero-point energy is applied. Vibrations in the solids are not treated. When energies are discussed, an absolute scale is used. "higher" always refers to being more positive, and "lower" always refer to being more favorable. Thus, higher adsorption or etching energies refer to adsorption or etching being less favorable, respectively.

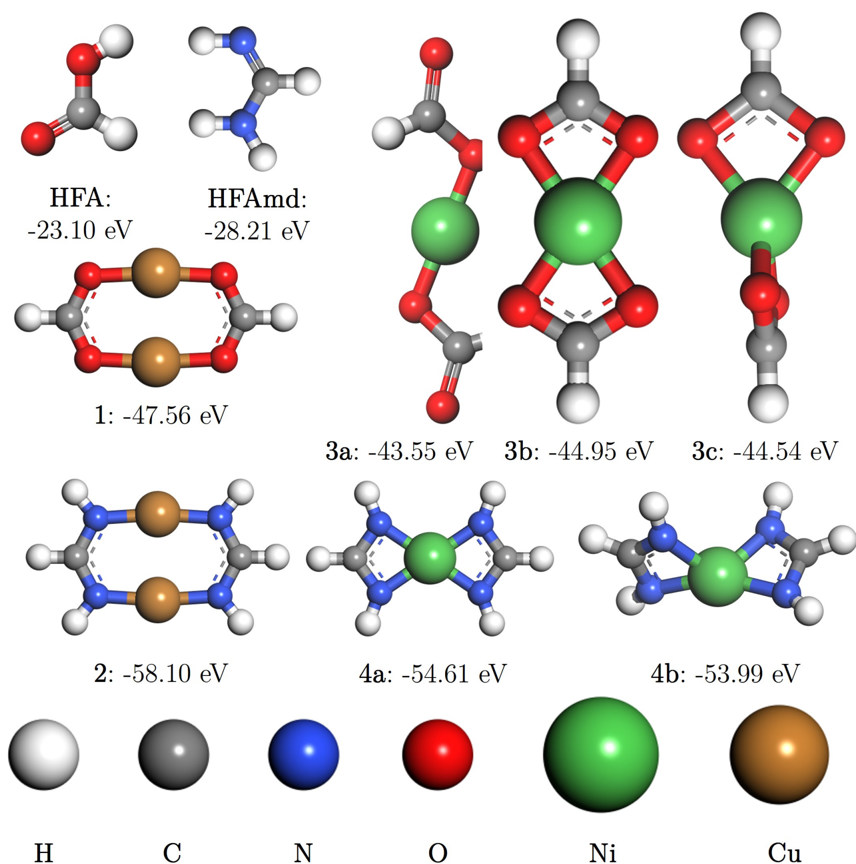

Figure 2.2: Relaxed structure models and electronic energies of unsubstituted metal complexes considered. **HFA,HFAmd**: Formic acid (HFA) and formamidine (HFAmd) etchants. **1,2**: distorted square planar copper formate and copper formamidinate complexes. **3a,3b,3c**: nickel formate in monodentate, bidentate planar and bidentate tetrahedral structures considered, respectively. **4a,4b**: nickel formamidinate in square planar and distorted tetrahedral structure, respectively.

CHAPTER 3

The bulk model

The first step to computationally screen ALE reaction chemistries is the development of an energy expression for the etching step. The first model in this thesis, the bulk model, is described here with the example ALE system composed of O_2 plasma, nickel, and formic acid as modifier, substrate and etchant, respectively. For the chemistry to be applicable, the following reaction must be thermodynamically favorable and occurs at a significant rate:

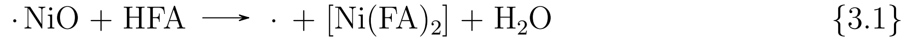

$$\cdot \mathrm{NiO} + \mathrm{HFA} \longrightarrow \cdot + [\mathrm{Ni(FA)_2}] + \mathrm{H_2O} \quad \{3.1\}$$

Equally important is that at the same time, the etch reaction on pristine nickel should be unfavorable or prohibitively slow:

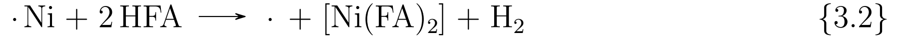

$$\cdot \mathrm{Ni} + 2\,\mathrm{HFA} \longrightarrow \cdot + [\mathrm{Ni(FA)_2}] + \mathrm{H_2} \quad \{3.2\}$$

In these and subsequent chemical equations, $\cdot$ indicates a surface species. At the basic level considered in this thesis, only thermodynamics are be assessed. The naïve expressions for Gibbs free energy change of etching reactions(etching energy) are the following:

$$\Delta G_{\mathrm{et,NiO}} = [G_{[\mathrm{Ni(HCOO)_2}]} + G_{\mathrm{H_2O}} + \cdot] - [G_{\cdot\,\mathrm{NiO}} + G_{\mathrm{HCOOH}}] \tag{3.1}$$

$$\Delta G_{\mathrm{et,Ni}} = [G_{[\mathrm{Ni(HCOO)_2}]} + G_{\mathrm{H_2}} + \cdot] - [G_{\cdot\,\mathrm{Ni}} + G_{\mathrm{HCOOH}}] \tag{3.2}$$

The term $G_{\cdot} - G_{\cdot\,\mathrm{Ni}}$ represents the energy cost of removing one nickel atom from the top layer. Likewise, the term $G_{\cdot} - G_{\cdot\,\mathrm{NiO}}$ is equal to the energy cost of removing one stoichiometric unit of nickel oxide. The bulk model simplifies the problem by assuming that the same pristine nickel/nickel oxide surface is exposed after one cycle. Therefore, the surface formation energies are unchanged, and surface effects cancel out each other. Under this

assumption, removing one atom from the surface is on average equivalent to bringing it out from the bulk lattice, energetically equal to the Gibbs free energy of formation of Ni(3.3).

$$G_{\cdot} - G_{\cdot\,\mathrm{Ni}} = -G_{\mathrm{Ni}}. \tag{3.3}$$

For the activated substrates(e.g nickel oxide), it is further assumed that the surface oxide has the stoichiometry and formation energy of the bulk oxide(Eqn. 3.4).

$$G_{\cdot} - G_{\cdot\,\mathrm{NiO}} = -G_{\mathrm{NiO}} \tag{3.4}$$

Thus the meaning of "bulk" is two-fold: the bulk formation energy is used for (1) pristine substrate, because same surface is regenerated and (2) activated substrate, because activation layer is assumed to take the bulk structure. The determination of all the terms appearing in equations 3.3 and 3.4 is described in Chapter 2. Substitution back into Equations 3.1-3.2 gives the etching energy expression in the bulk model. The combination of Ni/Cu substrate, N/O modifier, and formic acid(HFA) / formamidine(HFAmd)etchants results in eight potential ALE systems, listed in Table 3.2. The relevant chemical equations for all eight combinations of metal/modifiers/etchants are given in Rxn. 3.3-3.8.

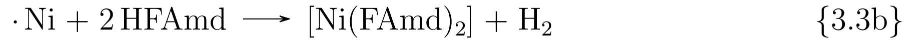

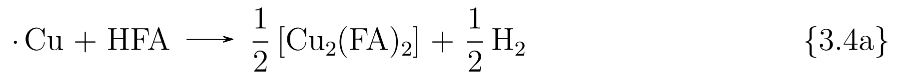

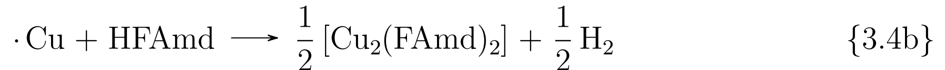

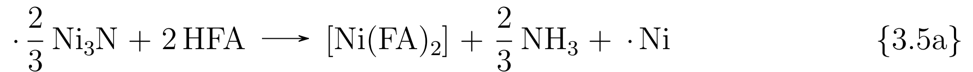

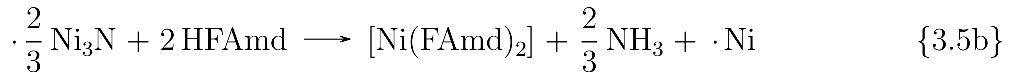

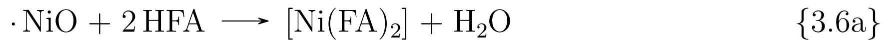

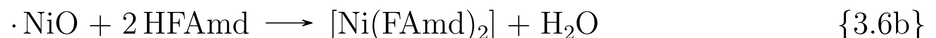

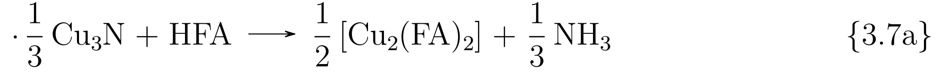

$$\cdot \frac{1}{3}\,\mathrm{Cu_3N} + \mathrm{HFA} \longrightarrow \frac{1}{2}\,[\mathrm{Cu_2(FA)_2}] + \frac{1}{3}\,\mathrm{NH_3} \qquad \{3.7a\}$$

$$\cdot \frac{1}{3}\,\mathrm{Cu_3N} + \mathrm{HFAmd} \longrightarrow \frac{1}{2}\,[\mathrm{Cu_2(FAmd)_2}] + \frac{1}{3}\,\mathrm{NH_3} \qquad \{3.7b\}$$

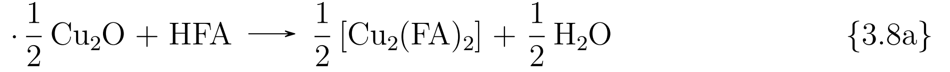

$$\cdot \frac{1}{2}\,\mathrm{Cu_2O} + \mathrm{HFA} \longrightarrow \frac{1}{2}\,[\mathrm{Cu_2(FA)_2}] + \frac{1}{2}\,\mathrm{H_2O} \qquad \{3.8a\}$$

$$\cdot \frac{1}{2}\,\mathrm{Cu_2O} + \mathrm{HFAmd} \longrightarrow \frac{1}{2}\,[\mathrm{Cu_2(FAmd)_2}] + \frac{1}{2}\,\mathrm{H_2O} \qquad \{3.8b\}$$

It is seen from Rxn. 3.3-3.8 that the balances for HFA and HFAmd are completely analogous. For brevity, reactions are not repeated for the two etchants from here on.

For Ni_3N etching, the stoichiometry of the complex and the nitride does not allow for a simultaneous removal of three Ni atoms per one N atom. There is a deficiency of nitrogen content on the bulk nitride substrate. Therefore, the etching would lead to either a nickel-rich surface, as indicated by the appearance of Ni atoms on the product side in Rxn. 3.5a-3.5b, or production of H_2, according to Rxn. 3.9

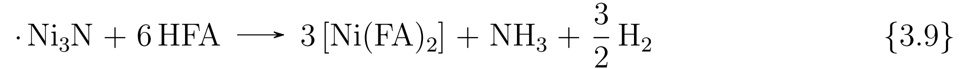

$$\cdot \mathrm{Ni_3N} + 6\,\mathrm{HFA} \longrightarrow 3\,[\mathrm{Ni(FA)_2}] + \mathrm{NH_3} + \frac{3}{2}\,\mathrm{H_2} \qquad \{3.9\}$$

The relative significance of the two competing reactions depend on μ_{N} and μ_{H}, the chemical potential of nitrogen and hydrogen, respectively. More explicitly, the position of the following equilibrium determines the relative importance of the two balances:

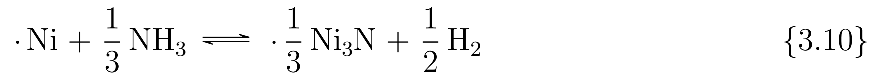

$$\cdot \mathrm{Ni} + \frac{1}{3}\,\mathrm{NH_3} \rightleftharpoons \cdot \frac{1}{3}\,\mathrm{Ni_3N} + \frac{1}{2}\,\mathrm{H_2} \qquad \{3.10\}$$

At the target process conditions, the free energy change of Rxn. 3.10 is +0.27 eV, favoring the left(reactant) side. At target process conditions, $\mu_{\mathrm{N}} = -8.5$eV due to the N_2 carrier gas. At this chemical potential, the Ni_3N phases are not thermodynamically stable under with trace amounts of H_2 presence. Depending on μ_{H}, the exposed terminations would be N/Ni(111), N/Ni(100), and N/Ni(210)[51]. It is therefore determined that Rxn. 3.10 heavily favors the reactant side, and Rxn. 3.5 is the preferred balance.

Note that the deficiency of nitrogen in Ni_3N(in fact, any stoichiometric "mismatch") is of no concern for the practical ALE process. It simply means that if $2l$ Ni layers are affected by the nitridation, only l layers of Ni would be removed, resulting in a lower etch-per-cycle. But the process remains to be alternating cycles of nitrogen plasma and etchants.

Table 3.1: Gibbs free energy of etching reaction on pristine substrates($\Delta G_{\mathrm{et,M}}$, Eqn. 3.1) from the bulk model, for Rxn. 3.3-3.4.

Substrate	Etchant	$\Delta G_{\mathrm{et,M}}$[eV]
Ni	HFA	1.61
Ni	HFAmd	2.07
Cu	HFA	0.58
Cu	HFAmd	0.50

The etching energies on the pristine substrates, $\Delta G_{\mathrm{et,M}}$, are shown in Table 3.1. Both Ni and Cu are expected to resist etching by HFA and HFAmd due to the large values of $\Delta G_{\mathrm{et,M}}$, making self-limiting reactions possible. The results on bare metal substrates involving HFAmd is expected since the amidinate complexes, substituted derivatives of the formamidinate complex, are used to deposit Cu and Ni in ALD [31]. The co-reactant reported is H_2, hence the reaction is the exact reversal of the ALE reaction. Overall, Ni has higher(more unfavorable) etching energies than Cu for the pristine substrate.

The etching energies of the activated substrates are given in Table 3.2. All four modifier and etchant combinations give a slightly favorable etching energy on Cu, although an etching energy of $\sim$ 0.1 eV is rather small. Etching on Ni with all four modifier/etchant combinations are positive(unfavorable). The calculated etching energy +1.51 eV of HFA etching Ni_3N is consistent with reports of Ni_3N deposition using amidinate complexes of nickel, although the ligands in the report are heavily substituted[30]. The result on Ni/O with formic acid (0.86 eV) is inconsistent with the experimentally observed etching[45].

The preferences for modifiers and etchants depend on the substrate. The oxygen modifier and formic acid are favored significantly by 0.20 eV and 0.45 eV, respectively, on the Ni

Table 3.2: Gibbs free energy of etching reaction on activated substrates($\Delta G_{\mathrm{et,MX}}$, Eqn. 3.2) from the bulk model, for Rxn. 3.5-3.8.

Substrate	Modifier	Etchant	$\Delta G_{\mathrm{et,MX}}$[eV]
Ni	N	HFA	1.06
Ni	N	HFAmd	1.51
Ni	O	HFA	0.86
Ni	O	HFAmd	1.31
Cu	N	HFA	−0.04
Cu	N	HFAmd	−0.11
Cu	O	HFA	−0.06
Cu	O	HFAmd	−0.13

Table 3.3: Difference of Gibbs free energy of etching on pristine and activated substrates, according to Rxn. 3.3-3.8.

Substrate	Modifier	$\Delta G_{\mathrm{et,M}}-\Delta G_{\mathrm{et,M}}$[eV]
Ni	HFA	0.56
Ni	HFAmd	0.75
Cu	HFA	0.62
Cu	HFAmd	0.64

substrate. On Cu systems, differences of 0.02 eV favoring oxygen and 0.07 eV favoring formamidine are not significant.

Table 3.3 lists the differences in etching energies on the pristine and activated substrates. This difference can be thought of as the energy window for the choice of etchants. On all combinations of metals and modifiers investigated, this difference is highly positive, suggesting these modifiers have the potential to allow for ALE. The difference of the Ni/O system at 0.75 eV is the highest of all the systems considered, consistent with the high selectivity demonstrated in the working Ni/O/HFA process.

The etching energies in Table 3.2 give the illusion that copper is more suited to the ALE processes considered here. It must be emphasized that the energies here is only for the etching step, with no bearing on the formation of nitrides and oxides. The ease of etching copper is offset by the difficulty to modify it, particularly with low-energy N_2 plasma. The easier the etching step, the more difficult the activation step.

Energy decomposition gives additional insights. The reactions are decomposed into three imagined steps. In step a), substrates evaporate into metal atoms and, in the case of activated substrates, modifier atoms. In step b), metal atoms react with etchants to form complexes and hydrogen radicals. In step c), radicals combine to form the co-product(NH_3/H_2O/H_2). The steps must be not be understood as actual mechanisms, but as a construction to separate the effects of substrate, modifier, and etchant. The decomposed reaction steps are given in Rxn. 3.11-3.16 for the formamidine etchant. These reaction balances have been written to sum to the etching reaction of Rxn. 3.3-3.8 which are themselves written for a single atom being removed from the substrate.

$$\cdot\,\mathrm{Ni(bulk)} \longrightarrow \mathrm{Ni(atom)} \quad \{3.11a\}$$

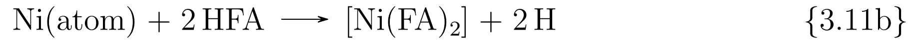

$$\mathrm{Ni(atom)} + 2\,\mathrm{HFA} \longrightarrow [\mathrm{Ni(FA)_2}] + 2\,\mathrm{H} \quad \{3.11b\}$$

$$2\,\mathrm{H} \longrightarrow \mathrm{H_2} \quad \{3.11c\}$$

$$\cdot\,\mathrm{Cu(bulk)} \longrightarrow \mathrm{Cu(atom)} \quad \{3.12a\}$$

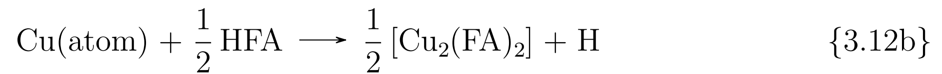

$$\mathrm{Cu(atom)} + \frac{1}{2}\,\mathrm{HFA} \longrightarrow \frac{1}{2}\,[\mathrm{Cu_2(FA)_2}] + \mathrm{H} \quad \{3.12b\}$$

$$\mathrm{H} \longrightarrow \frac{1}{2}\,\mathrm{H_2} \quad \{3.12c\}$$

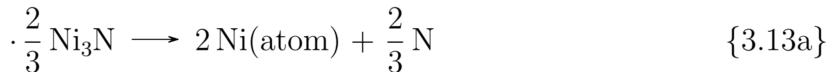

$$\cdot\,\frac{2}{3}\,\mathrm{Ni_3N} \longrightarrow 2\,\mathrm{Ni(atom)} + \frac{2}{3}\,\mathrm{N} \quad \{3.13a\}$$

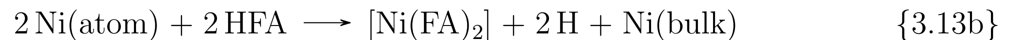

$$2\,\mathrm{Ni(atom)} + 2\,\mathrm{HFA} \longrightarrow [\mathrm{Ni(FA)_2}] + 2\,\mathrm{H} + \mathrm{Ni(bulk)} \quad \{3.13b\}$$

$$\frac{2}{3}\,\mathrm{N} + 2\,\mathrm{H} \longrightarrow \frac{2}{3}\,\mathrm{NH_3} \quad \{3.13c\}$$

$$\cdot \mathrm{NiO} \longrightarrow \mathrm{Ni(atom)} + \mathrm{O} \quad \{3.14a\}$$

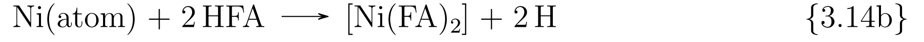

$$\mathrm{Ni(atom)} + 2\,\mathrm{HFA} \longrightarrow [\mathrm{Ni(FA)_2}] + 2\,\mathrm{H} \quad \{3.14b\}$$

$$\mathrm{O} + 2\,\mathrm{H} \longrightarrow \mathrm{H_2O} \quad \{3.14c\}$$

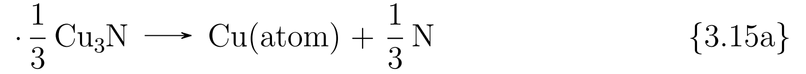

$$\cdot \frac{1}{3}\,\mathrm{Cu_3N} \longrightarrow \mathrm{Cu(atom)} + \frac{1}{3}\,\mathrm{N} \quad \{3.15a\}$$

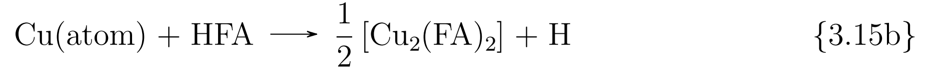

$$\mathrm{Cu(atom)} + \mathrm{HFA} \longrightarrow \frac{1}{2}\,[\mathrm{Cu_2(FA)_2}] + \mathrm{H} \quad \{3.15b\}$$

$$\frac{1}{3}\,\mathrm{N} + \mathrm{H} \longrightarrow \frac{1}{3}\,\mathrm{NH_3} \quad \{3.15c\}$$

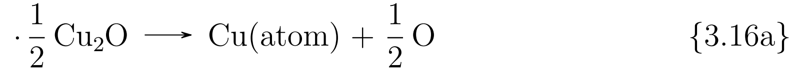

$$\cdot \frac{1}{2}\,\mathrm{Cu_2O} \longrightarrow \mathrm{Cu(atom)} + \frac{1}{2}\,\mathrm{O} \quad \{3.16a\}$$

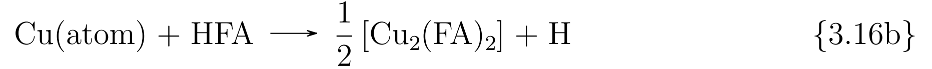

$$\mathrm{Cu(atom)} + \mathrm{HFA} \longrightarrow \frac{1}{2}\,[\mathrm{Cu_2(FA)_2}] + \mathrm{H} \quad \{3.16b\}$$

$$\frac{1}{2}\,\mathrm{O} + \mathrm{H} \longrightarrow \frac{1}{2}\,\mathrm{H_2O} \quad \{3.16c\}$$

The results of energy decomposition are shown in Table 3.4. Comparing the modifiers, on Ni substrate, it is seen that the $\sim$ 0.2 eV lower preference for O activation is due to the oxides binding being weaker than the nitride. Less energy is required to breakup the lattice, resulting in lower etching energy. For the Cu substrate, the oxides bonds are slightly stronger than the nitride bonds, but is canceled by the stronger stabilizing effect of water formation compared with ammonia formation(step c).

The fact that HFA etching nickel oxide films is possible suggests the real substrate could be quite different from the bulk nickel oxide. Depending on substrate conditions, the bulk model may or may not be suitable to describe a process. The bulk model lacks the flexibility to account for the variety of surface phases since it can only be limited to the few known bulk lattices. However, its simplicity makes it useful as a reference and sanity check for the more sophisticated models.

Table 3.4: Energy decomposition of bulk model. Step a, b, c correspond to the labels in Rxn. 3.11-3.16, and refer to bulk crystal decomposing, complex formation, and hydride formation, respectively. The energy values(in eV) is the Gibbs free energy per mole of reaction as listed.

Substrate	Modifier	Etchant	ΔG_{a}[eV]	ΔG_{b}[eV]	ΔG_{c}[eV]
Ni	Pristine	HFA	4.65	1.63	−4.67
Ni	Pristine	HFAmd	4.65	2.08	−4.67
Ni	N	HFA	12.70	−3.02	−8.62
Ni	N	HFAmd	12.70	−2.57	−8.62
Ni	O	HFA	9.52	1.63	−10.30
Ni	O	HFAmd	9.52	2.08	−10.30
Cu	Pristine	HFA	3.49	−0.57	−2.34
Cu	Pristine	HFAmd	3.49	−0.65	−2.34
Cu	N	HFA	4.84	−0.57	−4.31
Cu	N	HFAmd	4.84	−0.65	−4.31
Cu	O	HFA	5.66	−0.57	−5.15
Cu	O	HFAmd	5.66	−0.65	−5.15

CHAPTER 4

Layer model

4.1 Derivation of etching energy expression

Surface conditions must be considered more explicitly to study the effects of adsorbates and faceting. To develop the model in a straightforward manner, the same Ni/O/formic acid system is used as the working example below.

In contrast to the bulk model, the layer model has the ability to describe the cases where the surface oxide structure is significantly different from the bulk lattice. Although only surface adsorption is considered in this example application, the derivation of the etching energy is general. The only input required is a series of slab structures with their stoichiometries and energies.

The etching step in the layer model can be expressed as:

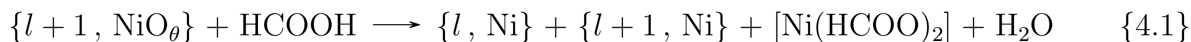

$$\{l+1\,,\, \mathrm{NiO}_\theta\} + \mathrm{HCOOH} \longrightarrow \{l\,,\, \mathrm{Ni}\} + \{l+1\,,\, \mathrm{Ni}\} + [\mathrm{Ni(HCOO)_2}] + \mathrm{H_2O} \qquad \{4.1\}$$

where $\{l+1\,,\, \mathrm{NiO}_\theta\}$ is the unetched, activated surface with $l+1$ layers of nickel, θ is the oxygen coverage(defined as the area density of oxygen atoms, in units of $\mathrm{\AA}^{-2}$). $\{l\,,\, \mathrm{Ni}\}$ and $\{l+1\,,\, \mathrm{Ni}\}$ are the pristine nickel surface with l and $l+1$ layers, respectively.

Following the bulk model, it is assumed that the essentially the same surface is exposed after one cycle of ALE. The difference is that here the surface after etching can exist in two thicknesses to accommodate for variable surface oxygen content. On the surface, etching starts near the adsorption sites, creating vacancies in the surface. The assumption is that the surface reconstructs to cover up the vacancies with atoms from other parts of the surface. The end result is large patches with $l+1$ layers and large basins with l layers, corresponding

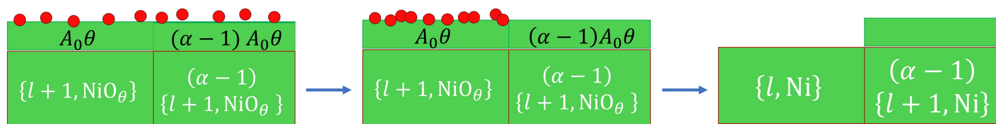

Figure 4.1: Imagined path to evaluate etching energies in the layer model. The modifiers are borrowed from other copies of the surface, leaving patches of unetched islands and etched basins. A_0 is the surface area, θ is area density of modifiers, so $A_0\theta$ is the number of modifiers on the slab. α is the total number of copies required to have enough modifiers to remove one layer on the original cell.

to $l+1$ and l terms on the product side of Rxn. 4.1. If islands are large enough, it is reasonable to neglect edge free energy and consider the island as the original surface with $l+1$ layers.

The stoichiometries for a full-layer removal is the same as in bulk model, listed in Rxn. 3.3-3.8. If the modifier on the surface is in deficiency, part of the layer would not be etched, existing as the $l+1$ term in Rxn. 4.1. The reverse case of deficient metal atoms(in the layers considered) is analogous: simply replace $\{l+1\,,\,\mathrm{Ni}\}$ terms with $\{l-1\,,\,\mathrm{Ni}\}$ in Rxn. 4.1.

In reaction thermodynamics, any path that connects the reactants and products can be used to evaluate the energetics. Conceptually, the path shown in Figure 4.1 is particularly helpful. In it, several copies of the unit cell is considered, and modifiers on other unit cells are borrowed to compensate for the stoichiometry needed to remove one layer. After etching, the lender surface with $l+1$ layers is unchanged, but the borrower surface now has l layers. The modeling of surface reactions, where the adsorption sites and reaction pathways must be considered in great detail, is therefore avoided.

Rxn. 4.1 is balanced in Rxn. 4.2. $\alpha = 1/\theta$ is the copies of modified surface needed to have enough modifiers to remove one layer of nickel atoms. Using Figure 4.1, the free energy change of the etching reaction is evaluated in Eqn. 4.2.

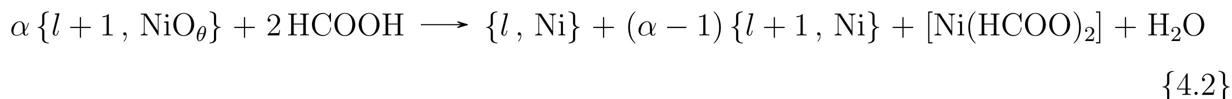

$$\alpha\,\{l+1\,,\,\mathrm{NiO}_\theta\} + 2\,\mathrm{HCOOH} \longrightarrow \{l\,,\,\mathrm{Ni}\} + (\alpha-1)\,\{l+1\,,\,\mathrm{Ni}\} + [\mathrm{Ni(HCOO)_2}] + \mathrm{H_2O} \qquad \{4.2\}$$

$$\Delta G_{\text{et}} = [(\alpha - 1)G_{l+1,\text{Ni}} + G_{l,\text{Ni}} + G_{[\text{Ni(HCOO)}_2]} + G_{\text{H}_2\text{O}}] - [\alpha G_{l+1,\text{NiO}_\theta} + 2G_{\text{HCOOH}}] \quad (4.1)$$

$$= \alpha(G_{l+1,\text{Ni}} - G_{l+1,\text{NiO}_\theta}) - (G_{l+1,\text{Ni}} - G_{l,\text{Ni}}) + (G_{[\text{Ni(HCOO)}_2]} + G_{\text{H}_2\text{O}} - 2G_{\text{HCOOH}}) \quad (4.2)$$

The stoichiometric coefficients in Rxn. 4.2 and factors of Gibbs free energies in Eqn. 4.2 would depend on the substrate/modifier/etchant combination. Note that this stoichiometry is unrelated to the stoichiometry of the bulk nickel oxide but is determined by the valence of the nickel atom in the $[\text{Ni(HCOO)}_2]$ complex.

$$\Delta G_{\text{et}} = [\alpha(E_{l+1,\text{M}} - E_{l+1,\text{MX}_\theta}) - (E_{l+1,\text{M}} - E_{l,\text{M}})] \cdot \frac{1}{n^\circ_{\text{M}}} + (G_{[\text{ML}_\eta]} + \xi^*_{\text{X}} G_{\text{XH}_\chi} - \eta G_{\text{LH}}) \quad (4.3)$$

Eqn. 4.3 is the more general form of Eqn. 4.2. It accounts for the different stoichiometries of metal complexes and hydrides. $\xi_{\text{X}} = A_0 \theta_X / n^\circ_{\text{M}}$ is number of modifiers present on the surface for each metal atom. ξ^*_{X} is the number of modifiers required to etch one metal atom. $\alpha = \xi^*_{\text{X}}/\xi_{\text{X}}$ is the copies of the surface required to provide enough modifiers. η is the coordination number of the complex. $\chi = \eta/\xi^*_{\text{X}}$ is the number of hydrogen atoms in the hydride. n°_M is the number of atoms per layer in the slab structure(See Table 4.1). In the subscripts, LH refer to the etchant, XH_χ refers to hydrides, and $[\text{ML}_\eta]$ is the metal complex.

In Eqn. 4.3, the three terms in brackets can be assigned physical meanings. The first term is similar to the definition of adsorption energy minus referencing to μ_{X}. The second term is the energy difference of adding one layer to the slab model, and is equivalent to μ_{M}, the bulk formation energy of metal, when the surface energy(see Eqn. 4.6 and 4.10) is converged with respect to the number of layers. The third terms describes the bond breaking and formation of the etchant, hydride by-product, and metal complex). For a given substrate/modifier/etchant combination, the last two terms are constants. Everything about the surface oxide is expressed through the first term.

The layer model introduces, with the substrate effects, all the complexity required to describe it. The modeling of large surface structures is computationally more demanding than the bulk crystal. In addition, the surface can have infinitely many number of phases,

as opposed to a single bulk crystal phase. The different phases must be integrated to give a single etching energy that can be used to predict experimental findings. Since the sole input to the layer model is the structure and energy of the modified layers, the energetics obtained depends critically on whether the input structures are realistic.

4.2 Substrate definitions and adsorption site identification

Since Ni and Cu both have face-centered cubic(fcc) structures, their surfaces structures are similar. Seven terminations have been selected for this study, listed in Table 4.1. The choice is motivated by the need to have both terrace sites((100),(111)) as well as edge(211,221,311) and kink sites((210)). The choice for the surface supercells is motivated by the need to have roughly the same surface area on all the terminations. Potentially more stable structures(with a lower surface formation energy) could be found by sweeping through supercells, but getting the globally most stable configuration is not the focus. The same supercells are used for terminations on all four combinations of Cu/Ni substrates and N and O modifiers. An image for each supercell is provided in Figure 4.2. Table 4.1 also gives the number of atoms per layer on different terminations. This number is obtained by counting the number of atoms exposed in the vertical direction. These sets of atoms form the minimum repeating unit in the vertical direction, constituting "layers".

Without *a priori* knowledge on the surface conditions, the surface phases were modeled as single atoms adsorption structures. For a given coverage(defined as the area density of adsorbate atoms), many different configurations are possible, with a range of energies. The bulk of the computational effort went into determining these adsorption configurations. The author would like to point out that by design, this search approaches the most stable configuration, whereas the ions in the plasma has the potential to access configurations lying at higher energies(metastable structures). These structures represents the local minima of the Gibbs free energy in the configurational space. While it is true that given enough time they eventually undergoes phase change into the most stable configurations, their incorporation into the modeling is justified if their lifetime is greater than the process time scale. These

Table 4.1: Supercells used in configuration search. The pictures of the supercells are provided in Figure 4.2. n_{M}° is the number of atoms per layer, equivalent to the smallest vertical repeating unit.

Termination	Supercells	Surface area		n_{M}°
		Ni	Cu	
(100)	(3×4)	74.25	79.26	12
(110)	(3×3)	78.75	84.07	18
(111)	(3×3)	48.23	51.48	9
(210)	(2×2)	55.34	59.08	12
(211)	(2×2)	60.62	64.72	12
(221)	(2×2)	74.24	79.26	16
(311)	(3×2)	61.56	65.72	12

structures are considered briefly in Chapter 5.

To strike a balance between computational time and space sampled, a "site-enumeration" based configurational search scheme is used. The initial adsorption sites are determined by surface atom connectivity graphs to ensure uniqueness in their local chemical environment, while also adapted to surface supercell symmetry. For the atoms exposed in the topmost layer, each unique atom in the top layer defines one unique top site. Each unique pair of atoms defines a bridge site, etc. Starting with a bare surface, the adsorbate is added to the sites on the surface. A (3×3) bare supercell has one of each site, due to supercell symmetry. After relaxation, several sites coalesce to one chemically unique site. This happens for instance when top sites of three neighboring atoms are unstable and relaxes into the same three-fold hollow site. The initial adsorption energies, calculated by placing a single adsorbate, is given in Table 4.2 for all four combinations of metal and modifiers. The illustration of site positions is provided in Figure 4.2. The expression for adsorption energy is shown in Eqn. 4.4. μ_{X} is the chemical potential of the adsorbate. The Gibbs free energies of the surfaces

are approximated by their electronic energies. In the cases shown in Table 4.2, $n_{\mathrm{X}} = 1$.

$$\Delta G_{\mathrm{ads}} = (G_{\mathrm{MX}_\theta} - G_{\mathrm{M}} - n_{\mathrm{X}}\mu_{\mathrm{X}})/n_{\mathrm{X}} \approx (E_{\mathrm{MX}_\theta} - E_{\mathrm{M}} - n_{\mathrm{X}}\mu_{\mathrm{X}})/n_{\mathrm{X}} \tag{4.4}$$

A naming convention is needed in the discussion of adsorption sites. The naming is based on the coordination numbers and the position on the surface. When there is no ambiguity of position, 1,2,3,4-fold coordinated sites are be referred to as top("t"), bridge("b"), 3-fold hollow("3h"), and 4-fold hollow sites("4h"), respectively. Two types of 3-fold hollow sites exist, labeled as "fcc" and "hcp" following the convention in surface science. On higher-index terminations(e.g. (211)), the facet with larger surface area is termed step("s"), the other one termed counter-step("cs"). There are also the designations of trough("t") and peak("p"), both self-explanatory. For 3h sites on (211) and (221) the relative positions of high("h"), middle("m"), or low("l") of the site relative to the horizontal $xy-plane$ is attached(see the side views in Figure 4.2). The correspondence of names to labels is given in Table 4.2.

Table 4.2: Adsorption sites, labels, and adsorption energies (in eV) referenced to O_2 and N_2 at 80°C, 350 Torr. A blank cell means the site is not stable in relaxation and coalesced to other sites.

			ΔG_{ads}[eV]			
Termination	Site name	Site label	Ni/N	Ni/O	Cu/N	Cu/O
(100)	t	A1	2.43	−0.43	3.58	0.20
	b	A2	0.78	−1.63	2.15	−1.01
	4h	A3	−0.80	−2.34	0.56	−1.85
(110)	t-t	B5	0.24	−1.53	1.46	−1.09
	t-p	B4	2.42	−0.58	3.96	0.43
	sb	B2	0.81	−1.76	2.37	−0.87
	lb	B3	−0.05	−1.54	1.52	−1.14
	3h	B1	0.29	−1.80		−1.21
(111)	t	C3	2.58	−0.22	3.98	0.70
	3h-hcp	C2	0.11	−1.92	1.93	−1.00
	3h-fcc	C1	0.08	−2.04	1.85	−1.09

. . . continued

Termination	Site name	Site label	ΔG_{ads} [eV]			
			Ni/N	Ni/O	Cu/N	Cu/O
(210)	t-t	D6			2.23	−0.81
	t-p	D1	2.41	−0.70		
	b-t	D2	0.31	−1.59	1.88	−0.81
	b-p	D7	−0.48	−2.26	1.14	−1.55
	4h	D3	−0.06	−1.66	1.42	−1.20
	3h-1	D4	0.34	−1.67	1.42	−1.12
	3h-2	D5	0.34	−1.67		
(211)	t-s	E9	2.70			
	t-p	E1	2.46	−0.59		
	b-p	E2		−1.86		
	b-cs	E3	1.16	−1.22	2.35	−0.60
	4h	E4	−0.24	−1.82	0.98	−1.39
	3h-hcp-s-l	E6	0.28	−1.68	1.85	−1.07
	3h-hcp-s-h	E8	−0.04	−2.14	1.48	−1.45
	3h-fcc-s-l	E5	0.29	−1.62		−1.14
	3h-fcc-s-h	E7	0.24	−1.92	1.58	−1.30
(221)	t-t	F7	0.16	−0.58	1.29	
	t-p	F1	2.45		3.80	
	lb	F6	−0.09	−1.56	1.40	−1.07
	b-p	F2		−1.82		
	3h-hcp-s-l	F5	0.20	−1.83	1.74	−1.16
	3h-hcp-s-h	F3	0.13	−1.84	1.67	−1.17
	3h-fcc-s-m	F4	0.14	−1.91	1.61	−1.34
	3h-fcc-s-l	F10		−1.58		−0.98
	3h-fcc-s-h	F8	0.00	−2.18	1.39	−1.60
	3h-hcp-cs	F9	0.26	−1.85		−1.38
(311)	b-t	G2	1.17			−0.59
	b-p	G1		−1.88	2.23	
	4h	G3	−0.20	−1.80	1.12	−1.36
	3h-hcp	G4	0.08	−1.99	1.61	−1.33
	3h-fcc	G5	0.41	−1.61		−1.07

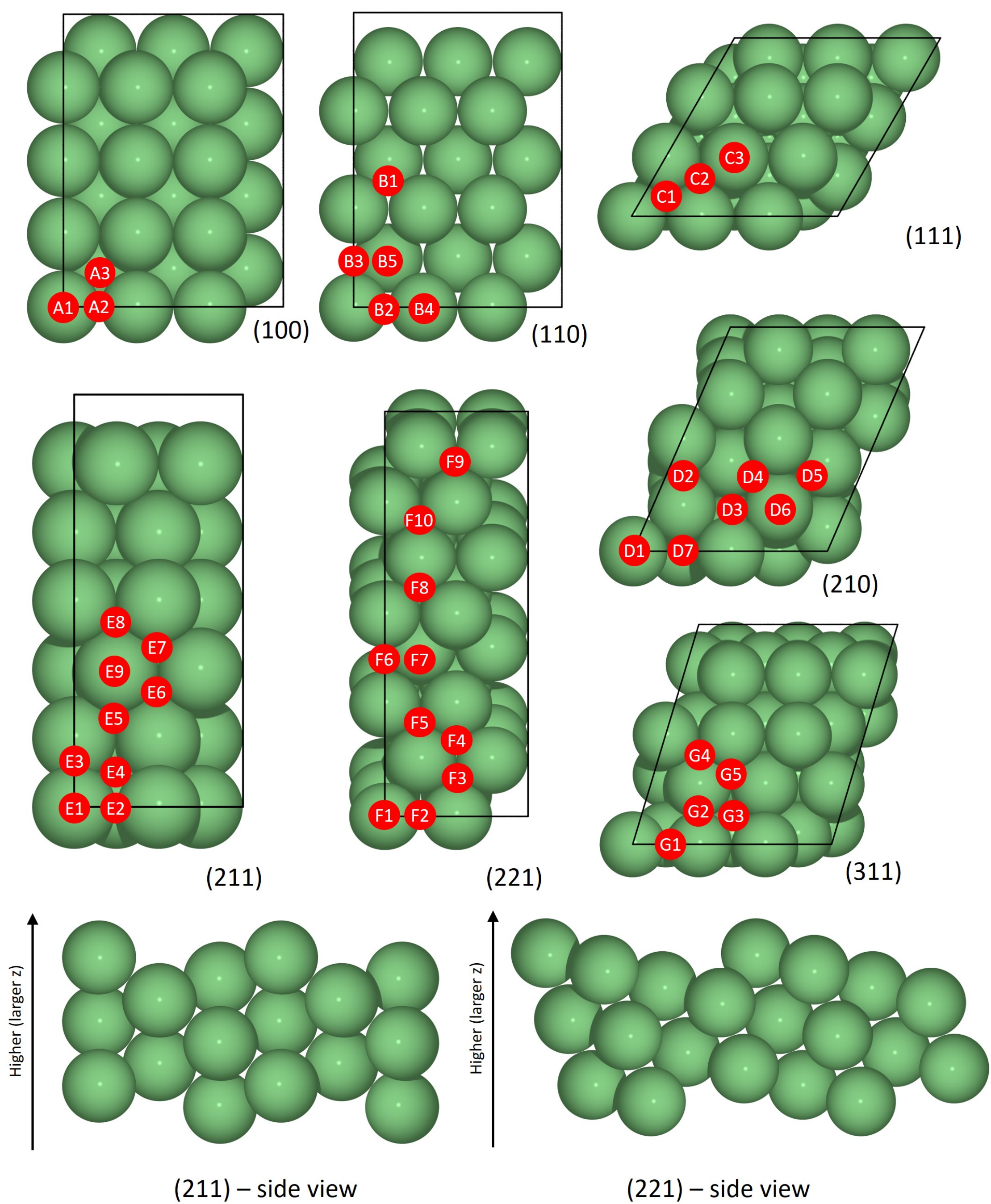

Figure 4.2: Adsorption sites on (100), (111), (110), (210), (211), (221), and (311) terminations of Ni and Cu. The supercells correspond to the actual slab model used in the configuration search. The (211) and (221) are shown in side view in addition to top view. Site labels are explained in Table 4.2

The comparison across modifiers shows that O gives a lower(more favorable) adsorption on Ni and Cu. Across the sites, this difference is not a constant. Adsorption energy on Ni/N "t-t" site on (221) is 0.74 eV higher than Ni/O "t-t" site, but the difference is 1.65 eV for the "lb" site and 2.03 eV for the "3h-hcp-s-l" site. Accordingly, site preferences of different adsorbates is not the same. On (100), O and N prefer "4h" site on Ni and Cu. But on (111), Ni/N prefers "lb" site, Cu/N prefers the "t-t" site, Ni/O and Cu/O prefer "3h" site. On low-index surfaces, the highly coordinated("3h" and "4h") sites are preferred. But on (210) surface, the low-coordinated "b-p" site is preferred by all modifier/substrate pairs.

It is interesting to compare adsorption energies for the similar sites. The (211), (221), and (311) terminations are composed of (100) and (111) vicinal terminations joined in steps. The chemical environment of "3h-fcc" and "3h-hcp" on these surfaces are expected to be similar to the "3h" sites on the (111) surfaces. Likewise, the "4h" sites are expected to be similar to the "4h" on the (100) surface. This is hardly the case. Consider the Ni/N system for example. The adsorption energies of 3h sites range from -0.04 eV to 0.29 eV on (211), from from 0 eV to 0.26 eV on (221), and from 0.08 eV to 0.41 eV on (221). In each case, the difference is ~ 0.3 eV.

Higher coordinated sites typically result in a more favorable adsorption energy because atomic adsorbates are used. These adsorbates can freely align their orbitals to maximize overlap with the orbitals substrate. However, this is not always the case. Consider the "4h" sites on (100), (211), and (311). The "4h" sites on (211) and (311) are on the step, but close to the counter-step, thus they have a (generalized) coordination number greater than 4h site on (100). Yet the adsorption energy of "4h" site on (100) is -0.80 eV, significantly more stable than any other sites on all terminations.

The complexity of this behavior suggests that geometric considerations alone(coordination numbers) cannot be used in the configuration search. In other words, the configuration formed by first occupying all of the most stable adsorption site is not guaranteed to be the most stable configuration.

4.3 Adsorption configuration search

After the sites have been identified, their adsorption energies are ranked in order. The most stable sites are selected into a pool, and another adsorbate atom is added to the previously most stable structure on these sites, effectively freezing the adsorption configuration from one iteration to the next. Care is taken to ensure around 10 unique candidates are present during each iteration, unless no more sites are available. Since the surface supercell is repeated, selecting a few candidate sites in the primitive cell already gives enough candidate structures for the first few iterations. Rotation and reflection symmetry elements of the supercell is considered such that equivalent configurations are not recalculated. Because initial selection of sites gradually become saturated as coverages become higher, new sites with a higher (less favorable) initial adsorption energy are included to compensate.

During the optimization, all adsorbate atoms and metal atoms in the first few layers in contact with the adsorbates are relaxed. The bottom layers are constrained to simulate a bulk lattice. Any structures where adsorbate atoms recombine to form N_2 and O_2 are removed from the candidate pool by a monitoring program which periodically checks the atomic positions during relaxation. If not removed, the recombined molecules slowly drift away from the top of the slab, making convergence very slow. Sometimes the slab undergoes reconstruction and adsorbate atoms can move far away from their initial positions, making it difficult to identify the sites, defined for the unreconstructed slab. In such cases, the original slab is restored before new adsorbates are added. Because the structures are generated automatically, inevitably some unreasonable structures are generated and escape the detection algorithm. In these rare cases the VASP geometry optimizer would fail because it cannot converge the forces. Structures that are indeed impossible are discarded.

For the N activated systems, the search is continued until either all sites become occupied or any addition to the surface results in a recombination event, whichever occurs first. The process is the same for O activated systems, but the search is not yet concluded.

The average adsorption energy is already defined in Eqn. 4.4. Choice of μ_{X} is inessential at the moment for only the relative magnitudes is important.

As with any global optimization problem, there is no rigorous guarantee that the optimal configuration at a given coverage can be found this way. To address this concern, experimentally known surface phases are included for comparison whenever such information is available(Table 4.3), unfortunately on oxide systems only. In these structures, the metal slab cannot be produced by vertically repeating the top layer, because metal atoms have been added(or removed, depending on the actual mechanism) from the unreconstructed surface. The adsorption energy must be redefined to account for the energy cost of this reconstruction. The adsorption energy for these structures are defined for example system in Eqn. 4.5.

Table 4.3: Experimentally observed surface reconstructions and adsorption superstructures for the Ni/O and Cu/O systems.

Substrate	Termination	θ_O [Å^{-2}]	Surface cell	Ref.	ΔE_{ads}[eV]
Ni	(100)	0.040	$p(2 \times 2)$	[4]	-2.36
Ni	(100)	0.081	$c(2 \times 2)$	[4]	-2.04
Ni	(110)	0.057	(2×1) missing-row	[52]	-2.15
Ni	(110)	0.076	(3×1) missing-row	[52]	-2.01
Ni	(111)	0.047	$p(2 \times 2)$	[36]	-2.08
Ni	(111)	0.062	$(\sqrt{3} \times \sqrt{3})R30°$	[36]	-1.81
Cu	(100)	0.076	$c(2 \times 2)$	[12]	-1.51
Cu	(100)	0.076	$(2\sqrt{2} \times \sqrt{2})R45°$	[12]	-1.51
Cu	(110)	0.054	(2×1) pairing-row	[12]	-1.63
Cu	(110)	0.071	$c(6 \times 2)$	[12]	-2.45
Cu	(111)	0.087	$p4$	[46]	-2.69
Cu	(111)	0.098	$p4 + O_F$	[46]	-1.06
Cu	(111)	0.076	$p4 + OCu_3$	[46]	-1.31

In Eqn. 4.5, the term $E_{\text{Ni,slab-toplayer}}$ refers to the slab formed by vertically repeating layers. N_{Ni} is the "extra" Ni atoms above the slab. The energy cost to bring metal atoms to

the surface is estimated to be the bulk formation energy of the metal, as in the bulk model.

$$\Delta E_{\mathrm{ads}} = (E_{\mathrm{Ni/O,slab}} - E_{\mathrm{Ni,slab-toplayer}} - N_{\mathrm{N}}\mu_{\mathrm{N}} - N_{\mathrm{Ni}}\mu_{\mathrm{Ni}})/N_{\mathrm{N}} \tag{4.5}$$

Because atoms(radicals) are used in the configuration search, instead of dimers, the search is similar to the activation step in plasmas. Below, the similarity is exploited to discuss briefly the activation step. In Figure 4.3 the adsorption energies of oxygen and nitrogen on copper and nickel surfaces is given as functions of coverage, measured in number of modifier atoms per Å^2.

The general trend in all four combination is that the adsorption energies tend to increase(less favorable) with increasing coverage. The reason is two-fold. First, the most stable sites are occupied first by our explicit requirement. Sites that are still available at high coverages are not as stable as the first few adsorbates, hence the increased adsorption energy. The secondly reason is the repulsive lateral interaction among adsorbates.

There are notable exceptions to the this “rule”. A particularly pronounced case is the Cu/N system. Initially, average adsorption energies on all facets decrease or stay roughly constant. The structures at each iteration along the configuration search is given in Figure C.2. A closer look at the relaxed structures corresponding to the “dip” reveals that these structures have N atoms embedded into the top layer, some even reaching into the sublayer interstitial sites. The presence of surface nitrogen weakened the metallic bonds of the surface Cu atoms. The migration into the sublayer occurs as the adsorbates try to minimize the lateral repulsion by maximizing the adsorbate-adsorbate distance. Hence, a trend toward lower adsorption energies is seen initially. Eventually, the lateral repulsion at high coverages restores the increasing trend. A similar trend, although less pronounced, is seen for Cu/O near 0.05 Å^{-2}.

The initial decrease in adsorption energies is absent on the Ni surfaces. This is attributed to the fact that Cu is more malleable than Ni. The bulk modulus of Cu is 140 GPa, while that for Ni is 180 GPa[17]. Our calculations also indicate Ni bonds more strongly than Cu in its crystalline form.

The positive values of nitrogen adsorption energies indicate that the adsorbates are not

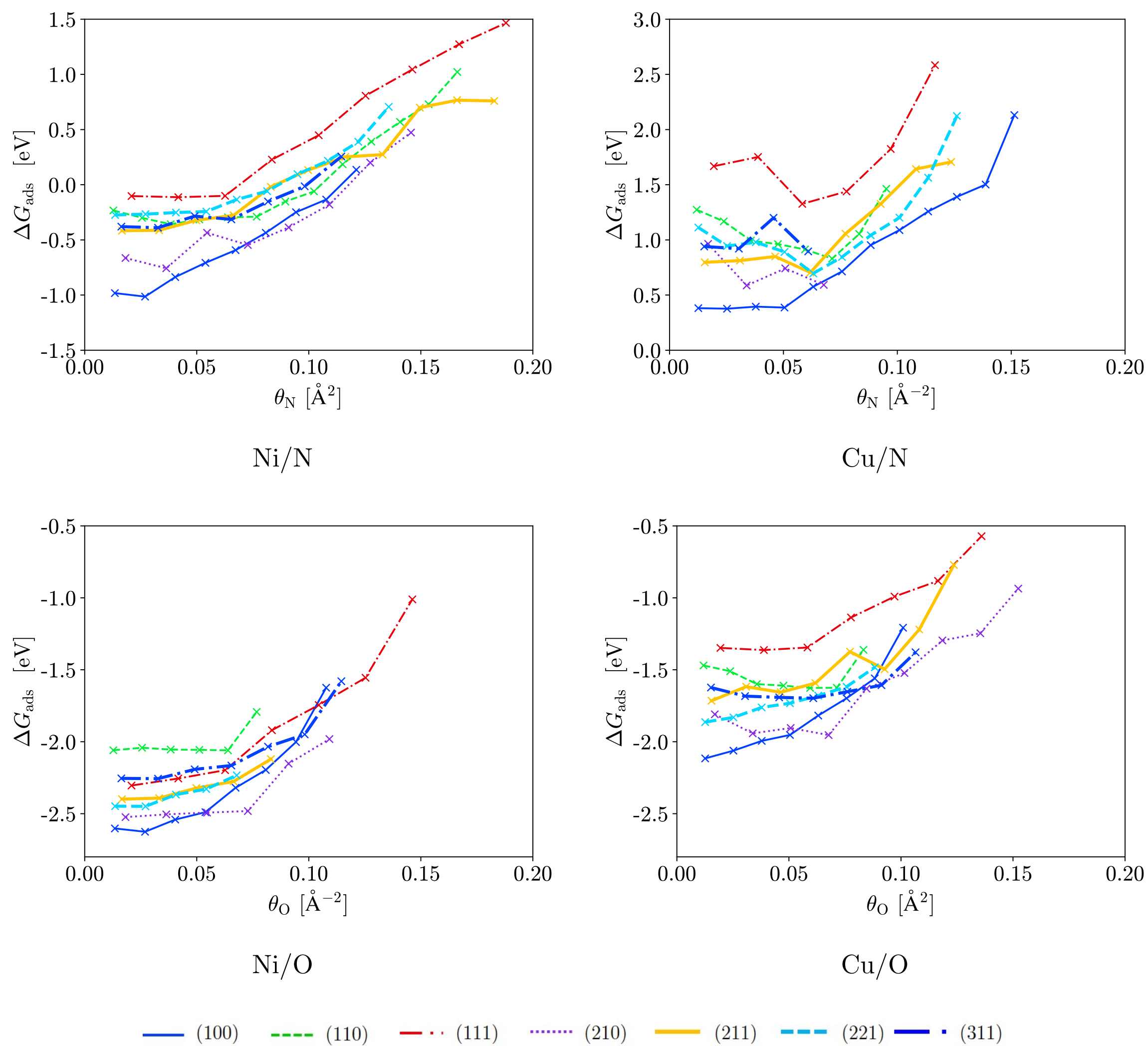

Figure 4.3: Adsorption energies of different terminations of the Ni/N, Cu/N, Ni/O, Cu/O systems as a function of coverage, referenced to N_2 and O_2 at 80°C and 350 Torr.

stable with respect to recombination to N_2 on Ni and Cu at the target process conditions of 80°C and 350 Torr. The practical implication is that if nitrogen is used as the modifier, it must penetrate the surface deeper than the adsorption structures to create thicker surface nitrides, as the adsorbates would readily desorb without a large kinetic barrier. The O adsorption on both substrate is favorable for all sites considered. A different problem exists: if the adsorption is too favorable, the oxygen/water present during vacuum break may oxide the pristine parts of the surface, lowering the selectivity.

As expected, copper is much more resistant to modification than nickel. The adsorption energy on Cu is ~ 1.5 eV higher than that of Ni for nitrogen. A similar but smaller effect of ~ 0.5 eV is present for oxygen. In Chapter 3 it was stated that from the etching energies(bulk model) alone, copper seem more suited to ALE. Although a positive energy for nitrogen adsorption does not rule out the process(since the references are diatomic gases), this advantage is offset by the potential difficulty in obtaining a stable nitride/oxide on the surface.

The termination of the adsorption can be discussed for N-activated systems. It is seen that Ni/N system on average saturates later the Cu/N system. On Ni/N, surface is saturated at an average 0.14 Å^{-2}, while that on Cu/N is 0.10 Å^{-2}. None of the O-activated is saturated at the coverages searched, suggesting the potential coverage reachable can be much higher.

There is some consistency among the terminations across the four systems. (100) gives the most favorable adsorption on all four systems at low coverage. As (100) becomes saturated, (210) adsorption becomes close to that of (100). The close-packed (111) surface gives highly unfavorable adsorption(for the case of Ni/N and Cu/O, the most unfavorable).

The adsorption of oxygen on Cu and Ni in the experimentally known configurations are listed in Table 4.3. A comparison to Figure 4.3 reveals that the non-reconstructed surfaces have adsorption energies that are either on or slightly above the curve(e.g. Ni(100), Ni(111) and Cu(100)). The reconstructed surfaces (Ni(110), Cu(110)), are more stable compared to unreconstructed ones at the same coverage. The epitaxial oxide on Cu(111) are also calculated. The results indicate that they are much more stable than the adsorption structures

found by our algorithm. Since reconstructions are outside the search space, such deviations are expected. Based on these evidence, it is safe to conclude that our search algorithm gives reasonable configurations.

4.4 Etching energies by termination

The etching energies of each surface phase are shown in Figure 4.4. Note that two energies are shown, with formamidinate chemistry on the left y-axis and formic acid chemistry on the right. Since the stoichiometry is the same, the two differ by a constant offset.

For the Ni systems, the etching energies of different terminations are initially centered around the bulk value, corresponding to $\theta = 0$. For Cu systems, a large initial decline is observed. This is an artifact of the sudden change in chemical equation, and not to be understood as an actual discontinuity in the etching energy cost when the surface is sparsely covered by oxygen. At low coverages, etching is not possible given the large thermodynamic driving force in the other direction.

The curves for Cu is much more irregular than those for Ni, due to the malleable nature of the substrate. A particularly striking example is the Cu/N (111) termination, where an increase of about ~ 0.2 eV is observed. A similar increase is present for other terminations of the Cu/N, all at coverages around 0.07Å^{-2}. This behavior is largely missing from the Ni systems.

The general trend is the reverse of the adsorption energies. This is largely expected since the first term in etching energy(Eqn. 4.3) is the adsorption energy without the reference to μ_{X}. While adsorption energies increase with coverage, etching energies generally show the opposite. And just like the adsorption energies, there are exceptions where the $n + 1$ structure(n being number of adsorbates) is, averaged by the number of adsorbates, more stable than n. The reason is that either a potentially more stable structure was missed, or, as explained above for the Cu/N system, because higher coverage is required to access the more stable structure.

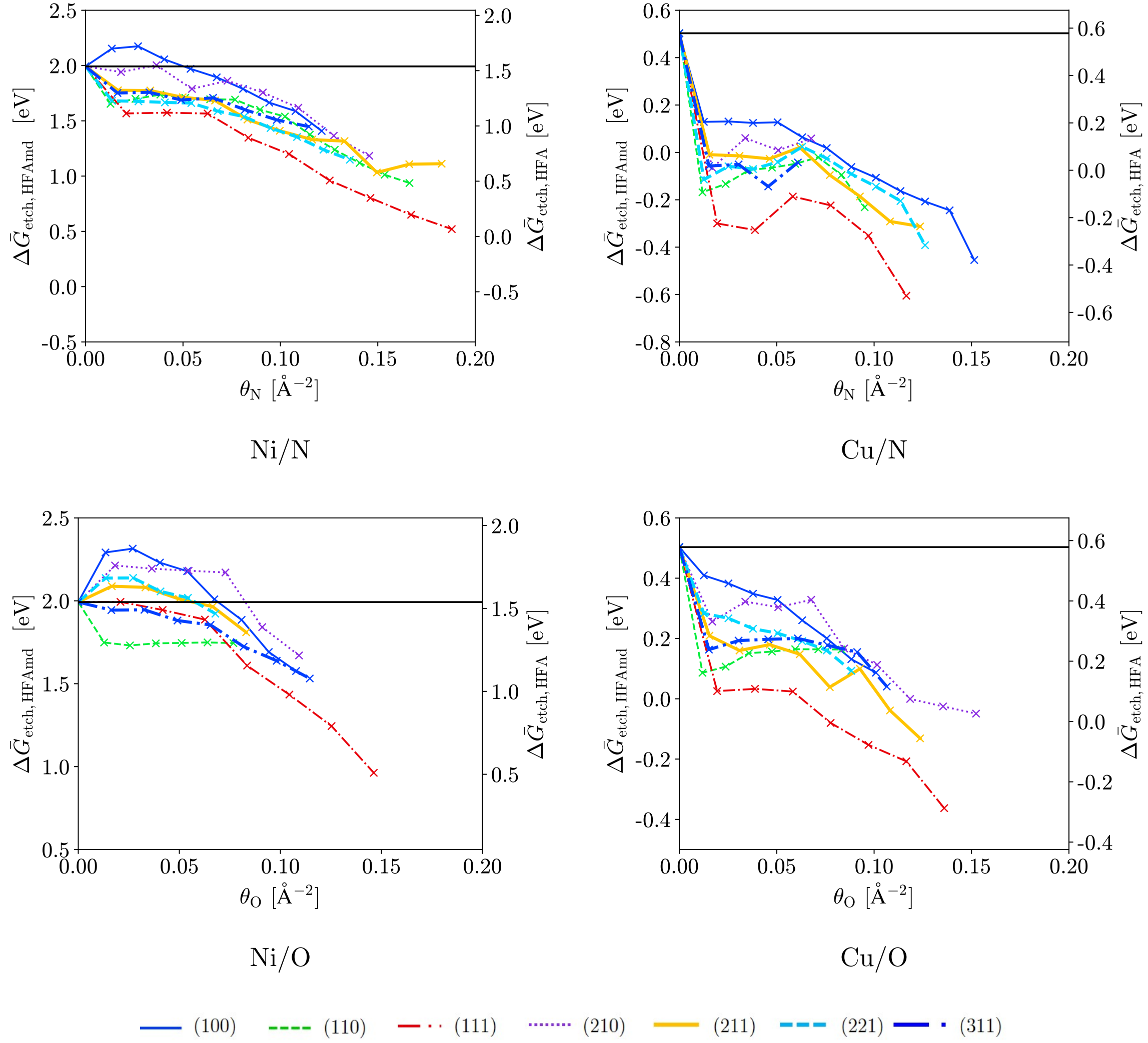

Figure 4.4: Etching energies of terminations on the Ni/N, Cu/N, Ni/O and Cu/O systems as functions of coverage. Two axis are shown. The y-axis on the left corresponds to formamidine chemistry. The y-axis on the right corresponds to formic acid chemistry. The horizontal bar represents the etching energy on the bare metal.

If the Langmuir adsorption model is followed exactly, every curve in the Figure 4.3 would be concave down, and every curve in Figure 4.4 would be concave up. The inflections of the actual curves indicate the non-ideal deviations.

At the saturation coverage of 0.18Å^{-2}, the Ni/N (111) surface is about to cross into being favorable for etching with formic acid, yet trend is stopped. It is reasonable to expect that if coverage is increased by occupying the subsurface interstitial sites, the trend could be continued and cross into being favorable. A similar fact is noted for Ni/O system, although here it is less conclusive because the surfaces are not saturated.

4.5 Determination of chemical potential and phase distribution

The etching energies of different terminations for a system cover a large range. At a given coverage, the difference between the most favorable and least favorable terminations is more than 0.5 eV for every system. It is difficult to interpret the myriad of etching energies. To proceed, one must somehow integrate etching energies on different terminations. The most reliable way is an average using experimental measurements of surface phase distributions, yet doing so is difficult, and contrary to the purpose of *in silico* process discovery. In the absence of such data, equilibrium crystal shapes are used to obtain the phase distribution. The input to this calculation is the surface free energies.

The traditional approach in characterizing surface conditions centers on the concept of chemical potential μ. Consider the case of a $\mathrm{NiO_x}$ surface. The surface formation energy γ is defined by:

$$\gamma = (G_{\mathrm{NiO_x}} - \mu_{\mathrm{Ni}} N_{\mathrm{Ni}} - \mu_{\mathrm{O}} N_{\mathrm{O}})/(2A_0) \tag{4.6}$$

where A_0 is the surface area. The factor of 2 is required because two surfaces are exposed in a slab model. At thermal equilibrium, the proportion of phases in equilibrium with the plasma depend on the relative magnitude of the surface energies. Higher μ_{O} leads to a preference for phases with higher oxygen content. The choice of the chemical potential depends on the physical situation. The surface is typically in equilibrium with a bulk material, in this case

bulk Ni crystal:

$$\mu_{\mathrm{Ni}} = G_{f,\mathrm{Ni}} = \text{bulk formation energy of nickel} \tag{4.7}$$

If the surface is exposed to an atmosphere of oxygen, then

$$\mu_{\mathrm{O}} = \frac{1}{2} G_{\mathrm{O}_2}(T, P) \tag{4.8}$$

In the oxygen plasma, due to the presence of various excited states, $\mu_{\mathrm{O,plasma}} > \mu_{\mathrm{O}}$, but the quantitative difference is difficult to determine. On the other hand, because the surface-plasma equilibrium is assumed, the state of the surface can be used to indirectly infer the condition of the plasma. Experimentally, the area density of the modifier atoms is easy to measure. At the coverage observed experimentally(the coverage that self-limiting adsorption stops at), no terminations should have a positive adsorption energy, leading to the indirect definition of chemical potential at saturation(Eqn. 4.9).

$$\mu_{\mathrm{O}}^{\mathrm{sat}} = \min_{\mathrm{facet}} \frac{E_{\mathrm{Ni/O}} - E_{\mathrm{Ni}}}{A\theta_{\mathrm{O}}^{\mathrm{sat}}} \tag{4.9}$$

where Ni/O refers to oxygen activated nickel surface. In other words, it is the minimum chemical potential required to reach the observed coverage. At this coverage, one surface phase(the one with minimum adsorption energy) is at equilibrium. The rest are past their saturation points. In reality, these other surfaces would not stay saturated at a lower coverage. Some form of reconstruction is likely to reflect the favorable chemical potential to increase the O content, but this is not explored here. The chemical potential calculated with Eqn. 4.9 is shown in Figure 4.5.

A correction must be made to Eqn. 4.6, the reason being that in asymmetric slabs only one side has adsorbates. The other side, also exposed to vacuum in the periodic simulation box, is essentially a pristine metal surface. The result of accounting for symmetry is shown in Eqn. 4.10. All the terms appearing in it have been determined. The resulting surface energies are shown in Figure 4.6.

$$\gamma_{\mathrm{Ni/O}} = (G_{\mathrm{NiO_x}} - \mu_{\mathrm{Ni}} N_{\mathrm{Ni}} - \mu_{\mathrm{O}} N_{\mathrm{O}})/A_0 - \gamma_{\mathrm{Ni}} \tag{4.10}$$

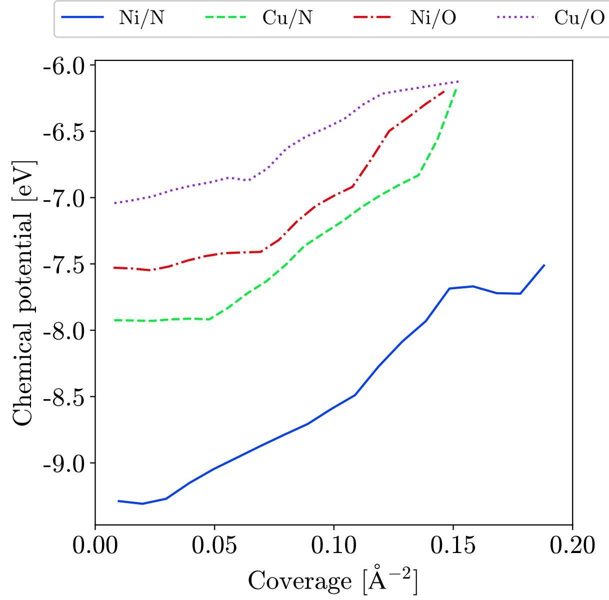

Figure 4.5: Relation of the chemical potential to the surface coverage(area density of modifier atoms), obtained from Eqn. 4.9.

On Ni/N, initially (111) is the most stable surface. At 0.025 Å^{-2}, (111) is overtaken by (100), which is saturated at $\sim$ 0.125Å^{-2}. At still higher coverages, (110), (210), and (211) compete for phase distribution. Ni/O system is dominated by (111) surface throughout the interval studied. The surface energy of (100) is immediately above it, followed by other higher index surfaces. Note that the vertical scale is different for each figure. Ni/N and Cu/O are very similar in that in both cases, (100) dominates most of the coverages. In Cu/O, (100) competes with (210) but in Cu/N, 210 surfaces is saturated very early, at a coverage of $\sim$ 0.06Å^{-2}. In Cu/O, the high-index surfaces including (311), (221), and (210) are close to (100), but in Cu/N, (100) dominates the phase distribution by far.

It is important to keep in mind that the surface energies in these plots are evaluated at a varying chemical potential, so comparison in the horizontal direction is meaningless.

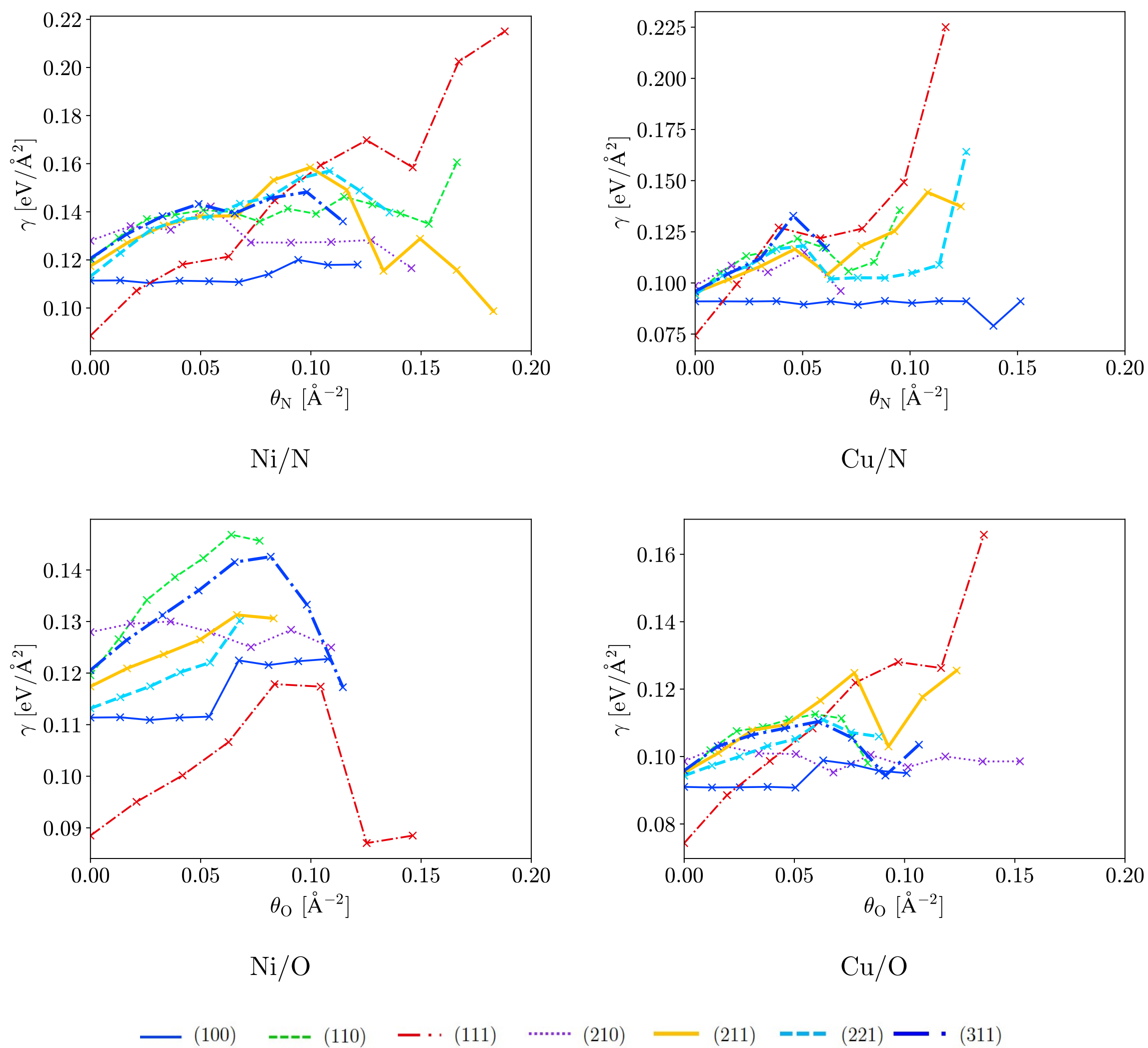

Figure 4.6: Surface energies of terminations on the Ni/N, Cu/N, Ni/O and Cu/O systems as functions of coverage.

4.6 Average etching energies

The etching energies on individual terminations are combined by distributions obtained in an equilibrium crystal shape analysis(Wulff constructions). Admittedly, Wulff construction is not consistent with our process because the constraint on the surface is fixed cross sectional area, different from the fixed total volume constraint in ECS calculations. It is selected nevertheless due to absence of a equilibrium surface faceting construction in the literature.

In the Wulff construction, some terminations that have low surface energies are not present in large proportions, due to geometric constraints. Wulffpack package is used in obtaining the phase distribution[43] as a function of the coverage θ. Interpolation is done on γ since the coverages for which a calculation is available is discrete and do not line up. Surfaces already saturated at a given coverage is not considered: no extrapolation is taken.

The average etching energies $\Delta\bar{G}_{\mathrm{et}}$, the final result of the layer model, are given in Figure 4.7. Four axis are shown. The axes on the left corresponds to the copper systems. Those on the left correspond to nickel systems. The chemistries corresponding to formic acid and formamidine are marked as HFA and HFAmd, respectively.

While it is true that surface oxides/nitrides, if thick enough, should reproduce bulk energetics(the assumption in bulk model), one must realize that the layer model is not meant to reduce to the bulk model, because the coverage for the most part is too low.

At the terminal points on the right of each curve in Figure 4.7, the average etching energies can be compared with the results from the bulk model. Readers are reminded that the oxygen configuration search is not complete, hence the terminal points in Figure 4.7 corresponding to O-activated systems do not represent the saturated surface structures.

All of the qualitative results of the bulk model on oxides and nitrides are reproduced. Etching Ni is shown to be unfavorable throughout the range of coverages, while etching Cu crosses from being unfavorable in the pristine system to become favorable for both systems. The bulk model predicts a −0.11 eV favorable etch for Cu/N/FAmd combination, while the terminal value in Figure 4.7 is −0.32 eV. The bulk model predicts Ni/N/FAmd combination to have 1.52 eV unfavorable etch, while the terminal value here is 1.11 eV. In both cases, the

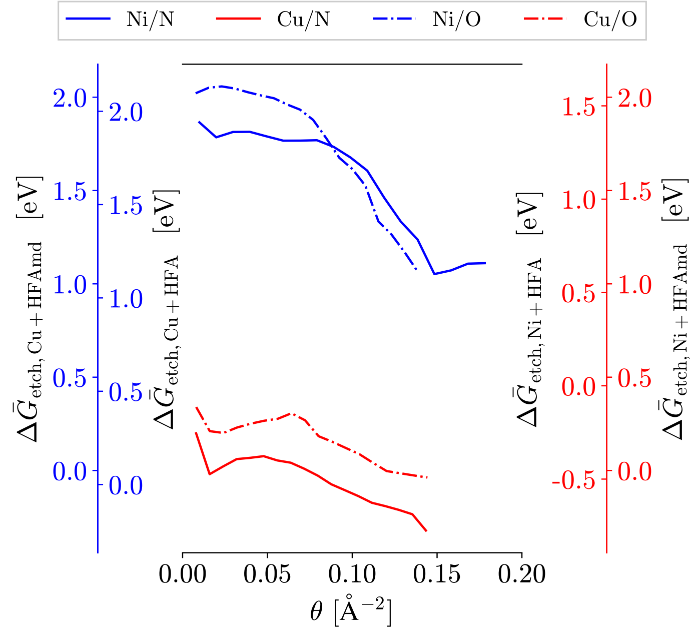

Figure 4.7: Wulff construction-averaged etching energies as functions of coverage.

etching of surface adsorption structures, as calculated by the layer model, is more favorable than the bulk model. The quantitative difference seem to depend the system.

The etching energies of Cu/O and Cu/N nearly parallel each other. The N-activated surface stays ~ 0.3 eV lower than the O-activated surface. Initially, both systems have a large decrease in etching energy. The rapid large decrease is followed by a slow increase, lasting about ~ 0.05Å^{-2} in range. Both systems then reach a peak etching energy, unfavorable to both etchants, before a rapid decrease is observed. The peak position is different. For Cu/N, the peak is observed at ~ 0.06Å^{-2}, whereas it is seen at ~ 0.07Å^{-2} for Cu/O. The etching energy on Cu/N system crosses over to become favorable for HFAmd at ~ 0.07Å^{-2}, the Cu/O system crosses at ~ 0.11Å^{-2}. The results for HFA are obtained by a shift and not repeated.

The Ni/N and Ni/O curves do not lie in parallel, although the two follows the same trend. A initial plateau is observed in both systems, followed by a slow decrease. At around the middle of each curve, the drop in etching energy becomes more rapid. Notably, the two curves can be seen as parallel curves shifted horizontally. There is an interesting fact

about the two curves: if the Ni/N curve is shifted to the left by $\sim 0.04\text{Å}^{-2}$, then they become nearly parallel, as in the Cu systems. The Ni/N system at low coverage is less favorable than the Ni/O system, but a crossover at 0.07 Å^{-2} with the Ni/N curve suggests that at higher coverages O is a better modifier, although it is inconclusive. Toward the end of Ni/N curve the etching energy increases again. This somewhat surprising result is explained by referring back to Figure 4.4 and 4.6. The termination responsible for the initial fast decrease is (111), but as its surface energy is raised, its proportion in the phase distribution is diminished with respect to the (211) and (110) terminations.

Although the configuration search on the Ni/O system is not yet finished, at the coverages searched, the etching energy is around 0.5 eV above the threshold to become favorable with formic acid. This etching energy, due to keep decreasing, is lower than that of the bulk model, but still unfavorable. Although further decrease is expected based on its similarity to the Ni/N curve, it is unlikely that the qualitative result would be changed. Hence, the surface adsorption structure also failed to reproduce the experimental results of Ni/O formic acid etching.

It is readily seen from the results of layer model that "atomic layer etching" cannot be strictly atomic layer, at least not for some substrates. To achieve the precise atomic layer removal, the activation have to be limited to the top layer. But for some substrates it might be difficult to find modifiers and etchants that gives a favorable etching energy at these coverages.

The layer model gives results that partially contradict experiments, but this is cannot be said to be a failure of the layer model itself. The structures in our configuration search is by design the most stable configuration at a given coverage and the Wulff construction average is a minimization of the total surface free energy. Hence, the estimates here is best considered as a conservative estimate, an upper bound of the actual etching energy.

CHAPTER 5

Ni/O/HFA process and metastable structures

Plasma ALE on the Ni/O/HFA system has been demonstrated. A sample of Ni thin films of $30 \sim 40$ nm in thickness were cleaned by Ar^+ sputtering, and then subjected to O_2 plasma. The presence of oxides was confirmed by X-Ray Photoelectron Spectroscopy. Film thickness change was measured by Scanning Electron Microscope(SEM) and Transmission Electron Microscope(TEM) to be ~ 6 nm after 2 minutes of exposure, significantly faster than the rate of native oxide formation. During the etching step, the sample is held at 80°C when formic acid is introduced to the chamber at pressures between 150 Torr and 550 Torr, with N_2 as the carrier gas. Exposure lasts 60 minutes with a 5-minute vacuum break between the activation and etching steps. Highly selective etching of NiO is reported. The selectivity of NiO to Ni is ~ 100, while that of NiO to hard mask(SiO_2) is essentially infinite. Etch rate at pressure of 350 Torr is calculated to be 0.1 nm/min. The oxidation is not self-limiting, since it produces 6 nm of oxide films, while the selectivity of NiO over Ni indicates the etching step is self-limiting.

In Chapter 4, the layer model was developed and applied to the case of activation by surface adsorption. In real plasma, on the other hand, the energetic ions are able to reach subsurface sites more easily than in thermal adsorption. It is therefore likely that metastable structures with lattice signficantly disrupted are present. To be clear, metastability refers to the local minima of the Gibbs free energy in the configurational space. Even though eventually these structures would be decomposed into the more stable global minimum, this process may be slow compared to the scale in ALE process. At the same coverage, these structures might be responsible for the favorable etching observed in the experiment.

Because the experiment uses the O/Ni/HFA combination, only the Ni/O system is con-

sidered when generating structures. Three nickel surfaces ((100), (111), and (211)) were selected since to represent the facet and edge sites present on polycrystalline surfaces. Given the small size of our slab model, the dynamics of lattice disruption in plasma processing cannot be simulated in DFT within reasonable computer time. The effect of such disruption is mimicked by placing the oxygen adsorbates into the subsurface interstitial sites, creating "sublayer structures". In a real oxidation process, some overlayer sites are likely to be populated first due to the kinetic barriers of accessing the sublayer sites. Therefore, structures with mixed occupation of overlayer and sublayer sites("mixed structures") are also included.

The overlayer sites are taken from the most stable site in Table 4.2. The subsurface sites are searched in a similar way, but many of the atoms placed into the sublayer are not stable by themselves, because the coverage is too low. After relaxation, these modifier atoms re-emerge to the surface and become identical to the modifiers in the overlayer sites. Only those sites stable under the relaxation are selected, their adsorption energies are shown in Table 5.1. For this reason, the low-coverage limit was not extended to the sublayer structure.

On (100) and (111), only the octahedral interstitial sites are present after relaxation. This is attributed to the fact that the Ni-O distance in the unrelaxed tetrahedral sites are too small. At 1.52Å, this is significantly less the sum of their Van der Waals radii(3.15Å). This close approach creates large forces, repelling the adsorbate atom back onto the surface. On (211), both tetrahedral and octahedral sites are present after the relaxation, but the octahedral site gives a lower adsorption energy. The adsorption energies are calculated with Eqn. 4.4, same as the overlayer structures.

Figure 5.1 shows the overlayer, mixed, and sublayer structures for the three terminations. Two limits of modifier density(coverage) were considered. The 1ML coverage corresponds to the saturated final state of the plasma oxidation process. These structures have the same stoichiometry(in the top layer) as the bulk NiO oxide. The low coverage case is taken directly from 4, corresponds to the case of placing a single modifier on a large substrate. The low-coverage case is not considered for the sublayer. The number of atoms in the layer is defined the same way as in Table 4.1, except here the supercells are smaller(see Figure 5.1).

Table 5.1: Adsorption energies of sublayer sites. The sites are generated by a displacement from the surface overlayer sites(parent site) in the direction perpendicular to the surface or step(on (211) only). ΔG_{ads} is calculated with Eqn. 4.4

Surface	Site	Parent site	ΔG_{ads}	Comments
(100)	octa	t	+1.06	
(111)	octa	3h-fcc	+0.40	half-embedded
(211)	octa	3h-fcc-s-1	+0.64	

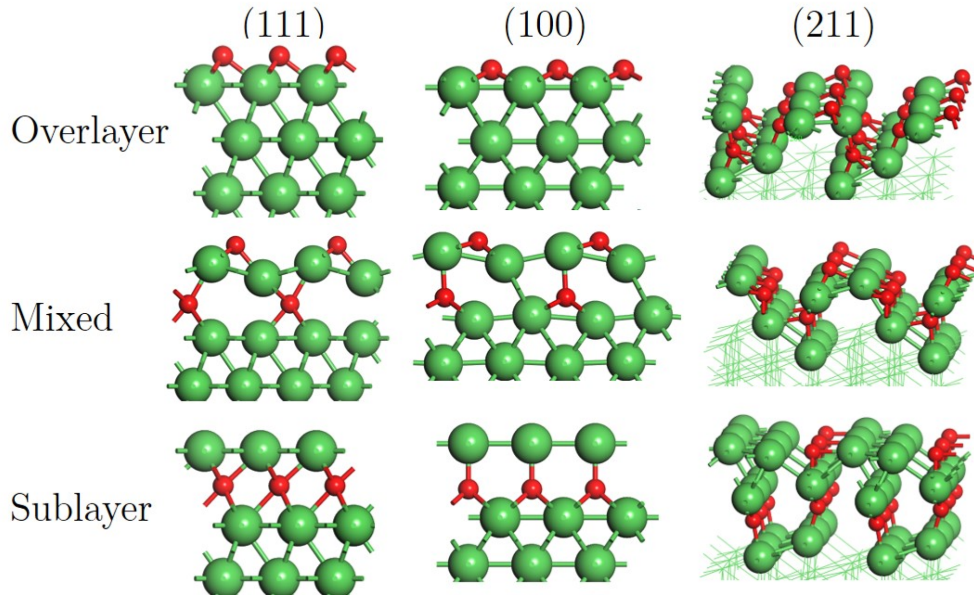

Figure 5.1: The relaxed structures of (100), (111), (211) surfaces with overlayer, mixed, and sublayer adsorption. (111) and (100) surfaces are shown in side view, (211) surface is shown in perspective. The green and red spheres represent Ni and O atoms, respectively.

The sites on the stepped (211) surface is difficult to see in Figure 5.1. While the overlayer and mixed structures initially had different site occupation, after relaxation they became very similar. Two types of oxygen atoms are present, namely 4-coordinated (4c) and 3-coordinated (3c). The overlayer structure has one 4c O atom and two 3c O atoms. The mixed structure shows two 4c O atoms (one in a square planar 4-fold hollow site, one in tetrahedral interstice site) and one 3c atom (in a triangular "(111) type" terrace site). The sublayer structure has only 3c O atoms.

The etching reaction energy is calculated with Eqn. 4.2. Figure 5.2 shows the etching energy of the activated surfaces. Only surfaces modified by a high coverage of oxygen, with occupation of subsurface sites and the formation of a surface NiO layer, result in a favorable etching reaction with formic acid, in agreement with experiments. Overlayer structures give consistently unfavorable etch, also noted in Chapter 4.

The site dependence trend is quite complex. For (111), increasing access to sublayer sites increasingly destabilizes the surface in a monotonic fashion, while (100) and (211) surfaces are not significantly destabilized by occupying a fraction of the sublayer sites in a mixed adsorption structure. (100) and (211) results indicate that occupying the sublayer sites using low energy oxygen ions can make the etching reaction favorable. A closer look at Fig. 5.1 reveals that etch becomes more favorable when Ni atoms in the top layer have a longer bonding distance with the layers underneath due to occupation by oxygen atoms in the sublayer. In particular, all the sublayer structures show a large vertical relaxation of the top layer, moving away from the bulk, while the mixed and overlayer structures still have one or more Ni atoms at short distances from the underlying metal. The geometry distortion caused by the oxygen modifier provides a favorable driving force. However, a more detailed search of the configuration space is required to validate this. Note that overall (211) has a higher(less favorable) etching energy compared with (100) and (111). This is attributed to the fact that while the(211) surface itself has a higher surface energy, occupying the under-coordinated sites on the edge initially stabilized the surface, to a higher extent than that of (100) and (111), where the terrace atoms have a higher coordination number. These results suggest that site specificity can play a role in atomic layer etching of surface species.

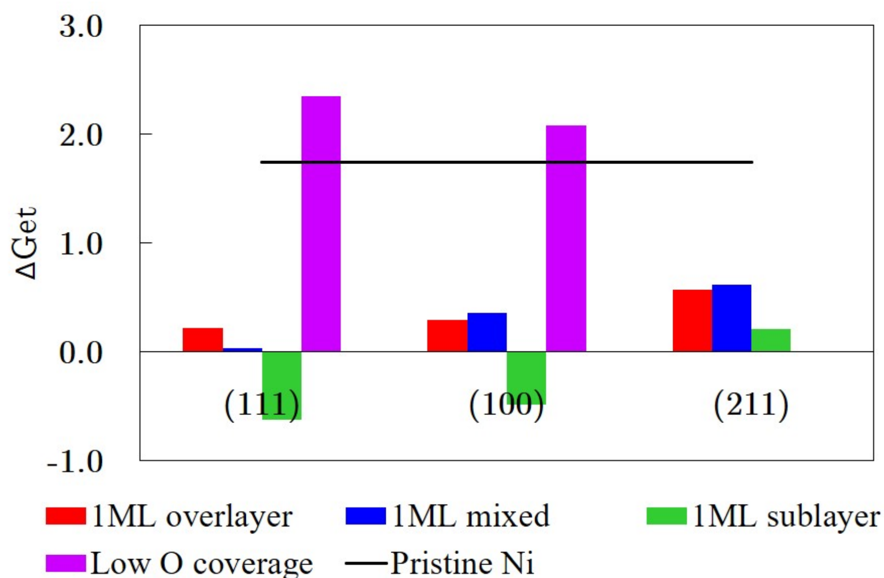

Figure 5.2: Etching energies of Ni/O system at overlayer, mixed, and sublayer structures.

A few differences exists between the experiments and the modeling. Although no direct structural characterization is available on the thin oxide films, at ~ 6 nm it is clearly not a surface adsorption process. The bulk model predicts an unfavorable etch, suggesting that the substrate formed by plasma oxidation does not have the structure of the bulk oxide. The layer model on the Ni/O system shows decreasing etching energy with respect to coverage, but at the coverages searched, it is still 0.5 eV away from being favorable. Here it is shown that metastable structures created by occupying the sublayer sites is able to result in an favorable etch.

When compared with the results in Chapter 4, it is seen that the success of the layer model depends critically on the knowledge of substrate conditions. A greater sampling of the structures resulting from lattice disruptions in a plasma activation process is required to expand the preliminary results obtained here.

CHAPTER 6

Summary and Conclusion

Atomic layer etching(ALE) is the technique poised to transform existing semiconductor manufacturing processes. At the ideal level, it uses time-separated steps of self-limiting surface reactions to achieve high selectivity, specificity, and anisotropy, at the same time opening up the process to many new, traditionally hard-to-etch materials. Existing research on ALE, although rapidly expanding in recent years, is still limited. The large chemical space of ALE, involving the antecedent choices of substrate, modifier, etchant, and process parameters, is impossible to exhaust by an trial-and-error approach. Research would rip a great benefit if a method is developed to allow for the fast screening of material systems. The first step towards this eventual goal, a computational model to evaluate the total etching thermodynamics, is not present in the literature.

Two models have been developed to address this problem. The applicability of the model on the O/N-modified Cu/Ni, with formic acid and formamidine etchants, is tested. In proposed processes, the etchant reacts with the modifier activated surface, creating metal complexes and a by-product hydride. To make reactions self-limiting, etchants must be nonreactive(unfavorable ΔG_{et}) on the pristine metal. The structures of the metal complex are proposed based on evidence found in the literature. Wherever evidence of a particular structure is missing or inconclusive, all candidates are examined and the most stable gas-phase molecule is accepted. The bulk lattice of the oxides/nitrides used in the study is selected based on the experimental evidence of their presence in thin films after plasma oxidation/nitridation of the metallic films. If such reports are lacking, the successful synthesis in thin films is taken.

Regarding the bulk model, all four combinations of metal and modifiers are resistant

to etch by both etchants. Under all modifiers/etchant combinations, etching is unfavorable on Ni and favorable on Cu. Comparing the etchants, formic acid is favored by 0.45 eV on Ni but disfavored by 0.07 eV on Cu. The choice of etchants appear to have no significant effect on Cu, but on Ni, the oxygen modifier gives etching energy more favorable by 0.20 eV. The difference in etching cost on the activated and pristine substrates is interesting as it can be used to characterize etching selectivity. This difference is highly positive on all four metal-modifier combinations, suggesting that these modifiers can used for ALE with suitable etchants.

The incorporation of substrate effects require the use of the layer model. In this model the new input is the surface slabs calculations. The etching energy is easily calculated by proposing an imagined where enough modifiers are brought to the unit area of the surface to allow for the stoichiometric removal of one atomic layer in the unit cell. Thermodynamically it is equivalent to assuming surface metal atoms have infinite lateral mobility on the etched surface. Surface adsorption sites are identified by symmetry, and the adsorbates are added to the surface one-by-one, keeping the configuration of the previous step. The adsorption energies of the resulting configurations are compared to experimentally known configurations. Excellent agreement is found. Etching energy on different terminations are averaged via surface phase distributions calculated from a equilibrium crystal shape.

The results of the layer model are eight etching energies as a function of coverage, one each for a modifier/substrate/etchant combination. The coverage, defined as the area density of the modifier, is used as a single descriptor for obtaining etching energies once the chemistry is selected.

Applied to surface adsorption structures, the layer model gives results that are qualitatively the same as the bulk model. At the highest coverage studied(the "terminal coverage), the Ni systems are unfavorable to etching, and Cu systems are favorable. The effect of etchant is independent of model and is already discussed above. The effect of modifiers from the layer model is different and richer than the bulk model. A large preference ($\sim$ 0.3 eV for the nitrogen modifier is observed on Cu system at all coverages studied, much greater than the bulk model prediction. On the Ni systems, at low coverages, the nitrogen modifier

is preferred by 0.3 eV, but the effect is reversed and at above $\sim 0.07\text{Å}^{-2}$, the oxide becomes the preferred activation layer.

The layer model clearly indicates that increasing coverage results in a more favorable etch. However, the number of sites on the surface is limited. The trend toward more favorable etching can be continued the coverage is increased. In the plasma activation process, significant surface lattice disruption due to the kinetic energy of the impinging ions is present. This effect is mimicked by creating structures with occupation of the subsurface interstitial sites. Several such structures were created for the Ni/O system, the resulting structure, once relaxed, shows favorable etching energies according to the layer model. Close examination of the structures reveals that those with a favorable etching energy is characterized by a large separation between the topmost metal layer and the bulk metal lattice, due to the steric repulsion of the modifier atoms.

Our modeling efforts can help ALE process development in the following ways. First, the effect of etchants can be separated from the rest of the process, if a careful study of the reactant and products are performed, as is done here. In particular, no experimental input is necessary for this aspect, which is a great advantage since more often than not the etching product is not well characterized. Second, the layer model clearly illustrates the importance of coverage. The results here suggest that the precise removal of one layer might be difficult in some metals because limiting the modifiers to the top layer results in low coverage.

The next step in the modeling of ALE thermodynamics is a consideration of plasma processing conditions. A correlation of plasma parameters to the surface structure will not only improve the structures fed into the layer model, but also potentially eliminate the approximations introduced by the Wulff construction average.

Appendix A

Computational details

The configurations search on Ni/N, Ni/O, Cu/N, Cu/O systems are done in two setups. At each step in the search iterations, the candidates for the next iteration are relaxed with a crude but fast computational setup. Because it is observed that the relative ordering of the candidates is not sensitive to plane wave cutoff, the most stable configuration can be found this way. Once the configuration is obtained, a second round of relaxation is launched to obtain accurate energies. Because geometry is already close to the final position, few ionic steps are required at the accurate setting, significantly reducing the computational cost. The crude search uses a Γ-centered $(3 \times 3 \times 1)$ reciprocal space sampling with 300 eV plane wave cutoff. The accurate setup for energies evaluation uses a $(5 \times 5 \times 1)$Γ-centered grid. Plane wave cutoff is 400 eV. All other parameters are identitical: energies are converged to 10^{-6} eV. Forces are converged to 0.02eV/Å. Second-order Methfessel-Paxton smearing is used to calculate partial occupancies, with smearing width equal to 0.2 eV. Dipole corrections are included in the simulations to offset the error introduced with asymmetric slabs. Gaussian smearing is used for isolated molecules, with smearing width of 0.01 eV.

Some molecular structures are optimized with the Gaussian 16 package. The basis set is chosen to be TZV on the metal atoms, and 6-31G(d,p) on the rest. B3LYP functional was used with "Tight" settings on geometry optimization and the self-consistent electronic structure calculations(Opt=Tight, SCF=Tight). The integrals are evaluated on an "Ultrafine" grid.

Appendix B

Structural parameters of the metal complexes

The bond lengths and bond angles of the complexes is shown in Table B.1, as optimized by VASP.

	$[Ni(FA)_2]$	$[Ni(FAmd)_2]$	$[Cu_2(FA)_2]$	$[Cu_2(FAmd)_2]$
M-N/O	1.911	1.909	1.874	1.862
N/O-C	1.281	1.324	1.275	1.328
M-M			2.477	2.587
N-C-N	116.054	108.489	128.309	123.848
N-M-N	110.698	111.818	174.407	172.498
N-M-N chelating	69.310	68.649		

Table B.1: Structural parameters of the organometallic complexes

Appendix C

Configuration search iterations

The relaxed structures at each step in the configuration search is are below.

100

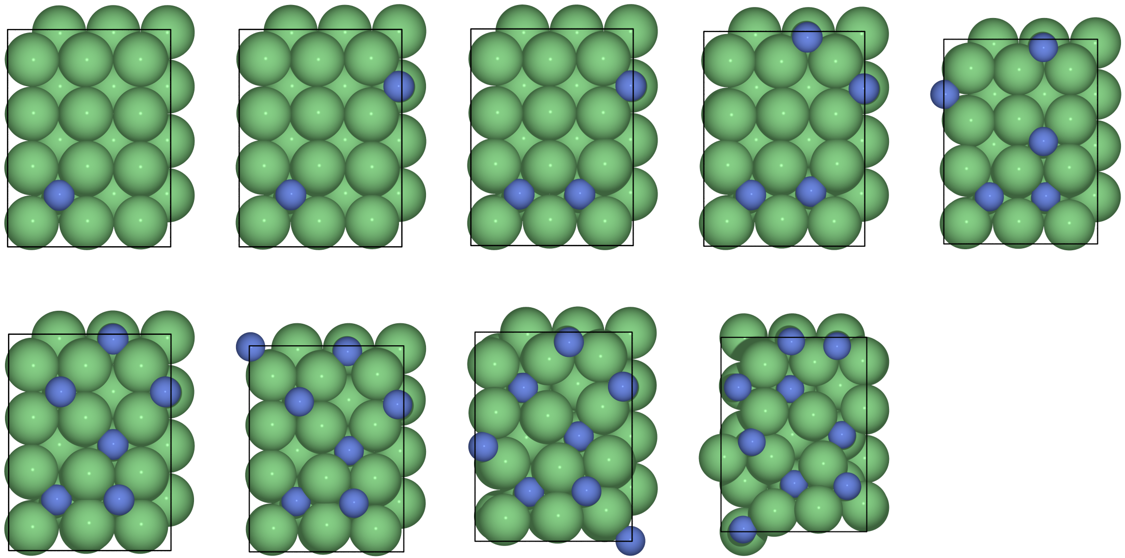

110

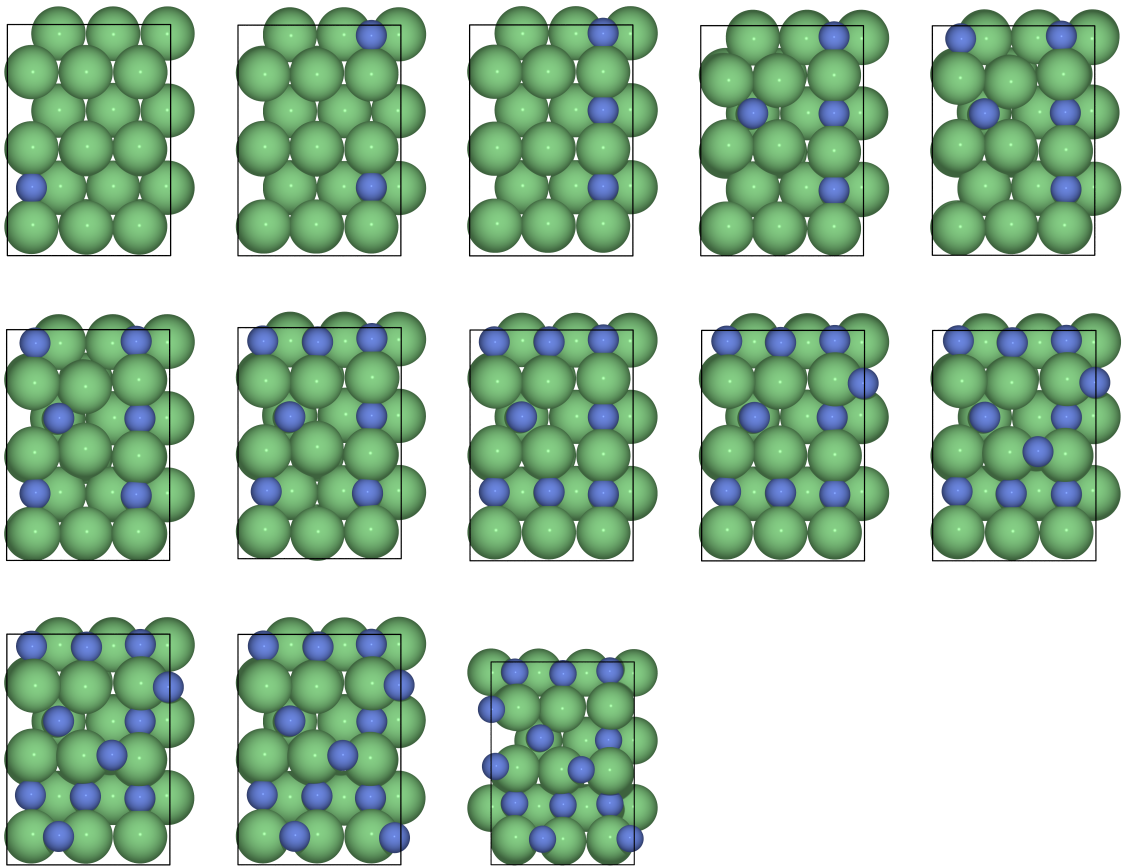

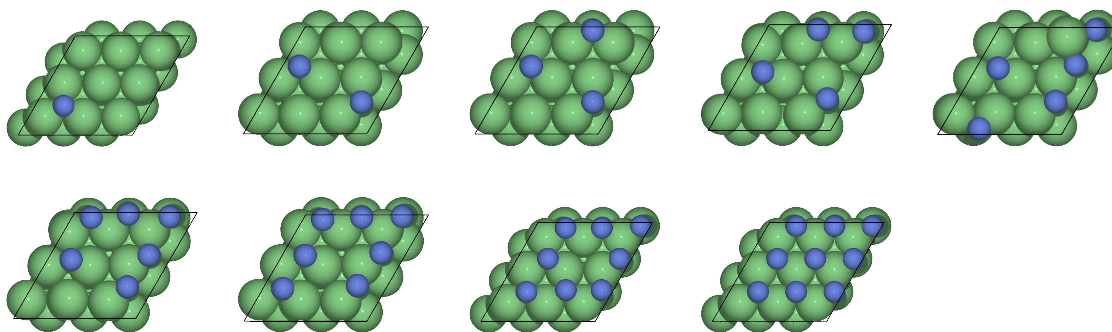
111

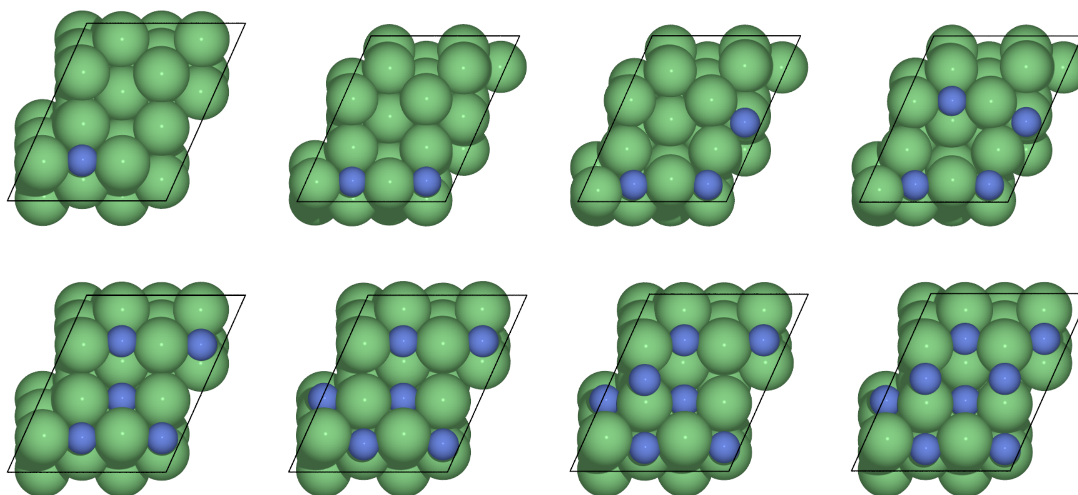
210

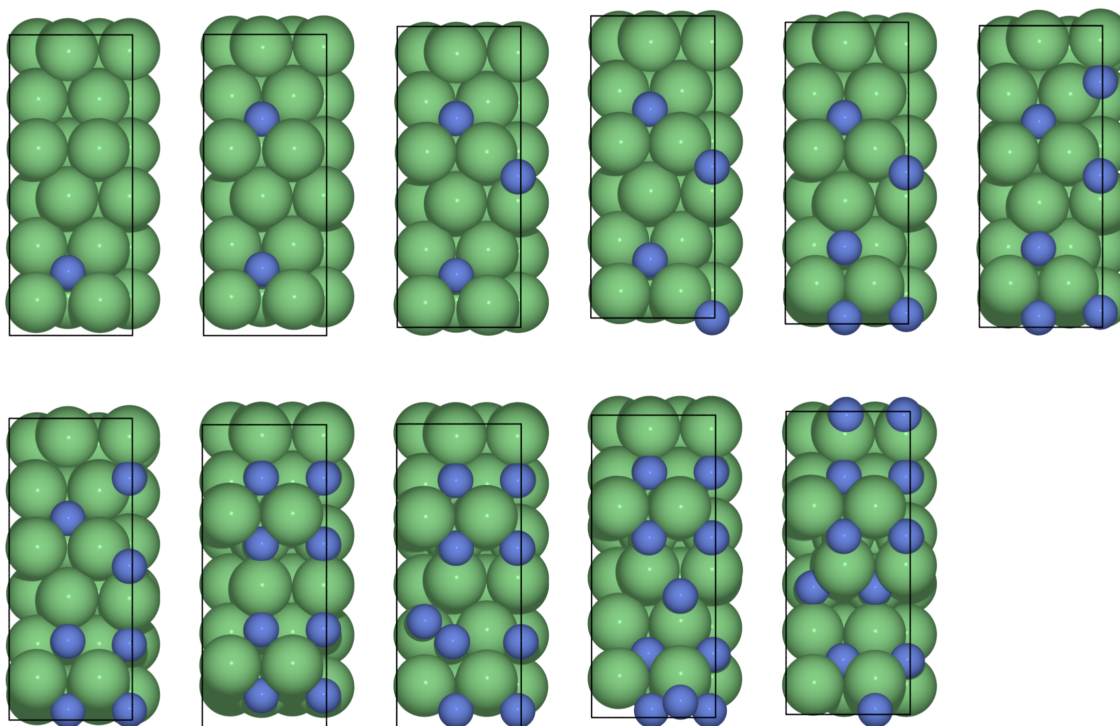
211

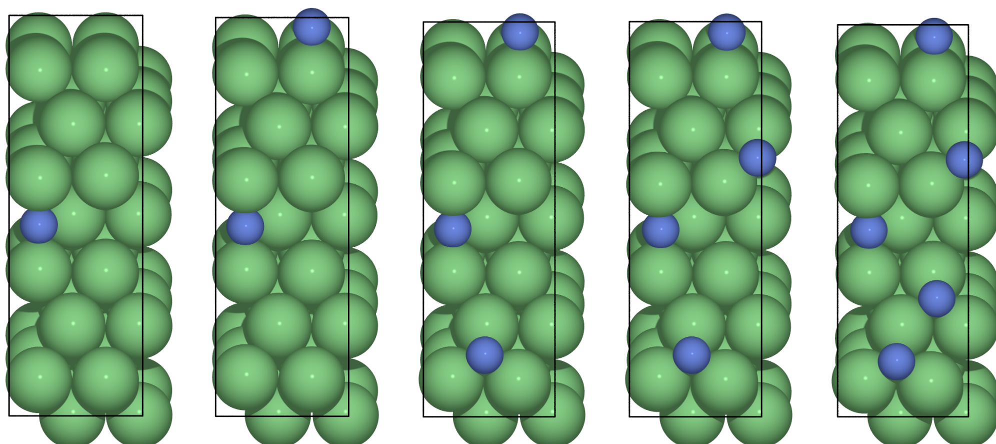

221

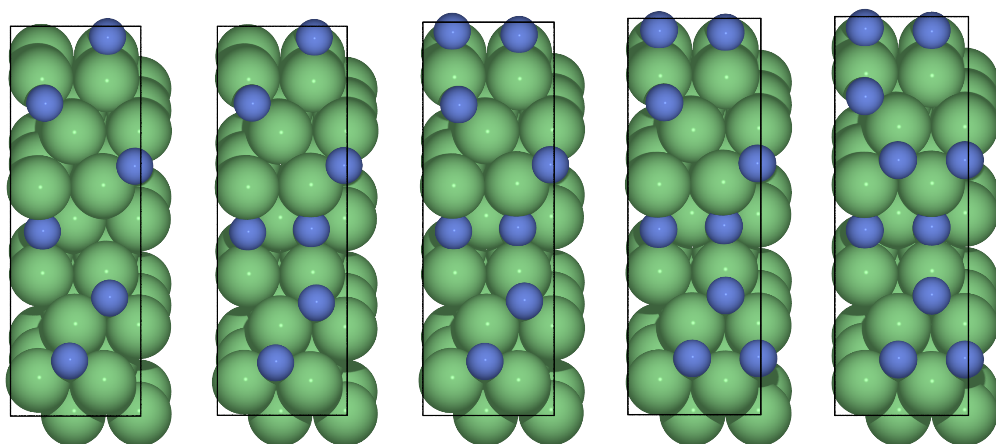

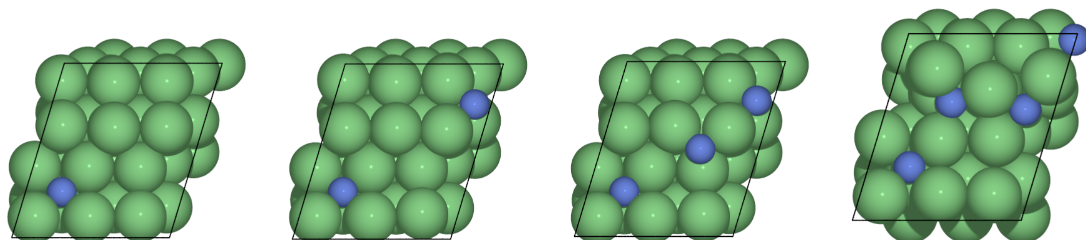

311

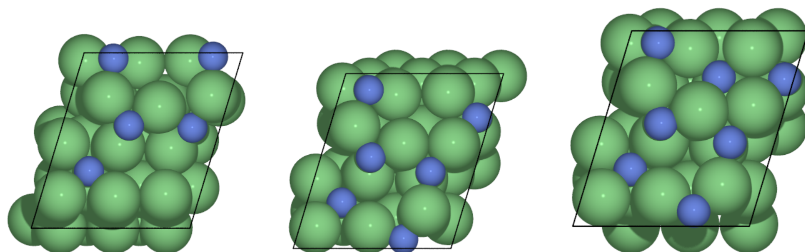

Figure C.1: Configuration search iterations for Ni/N system

100

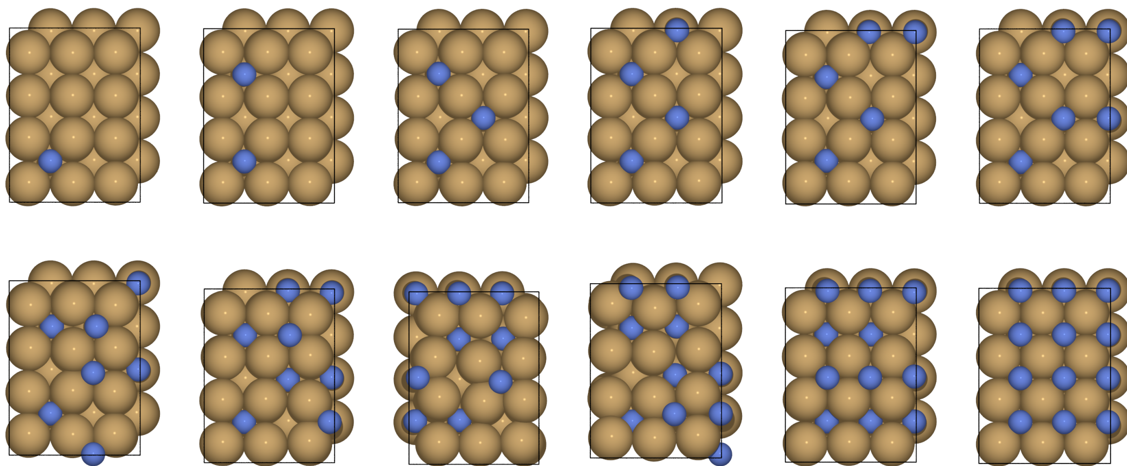

110

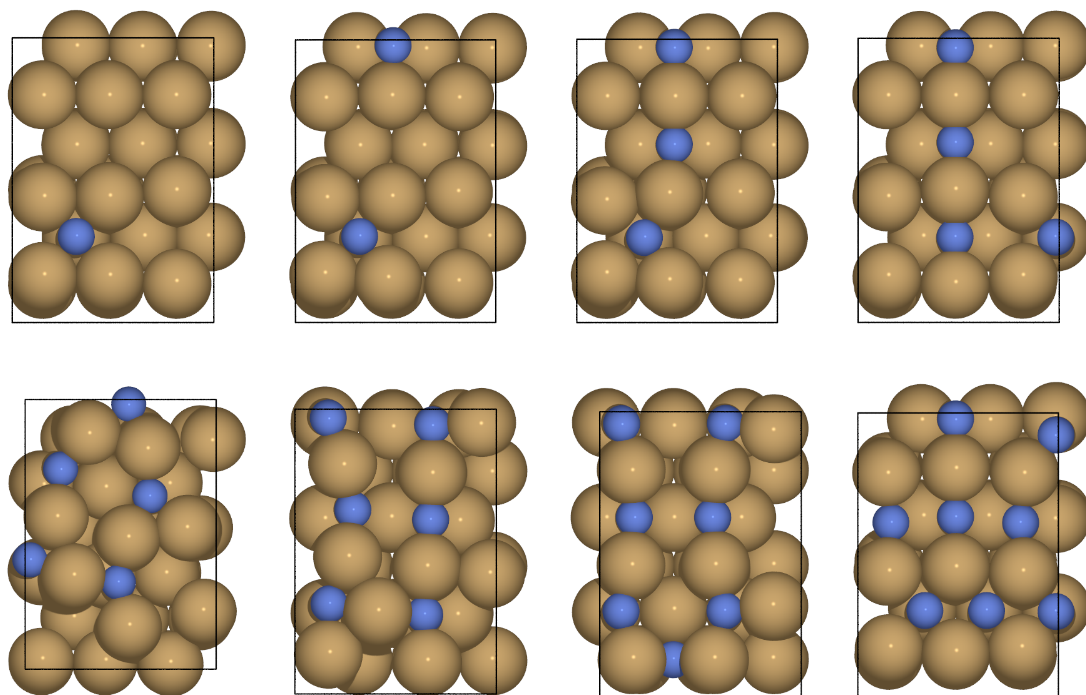

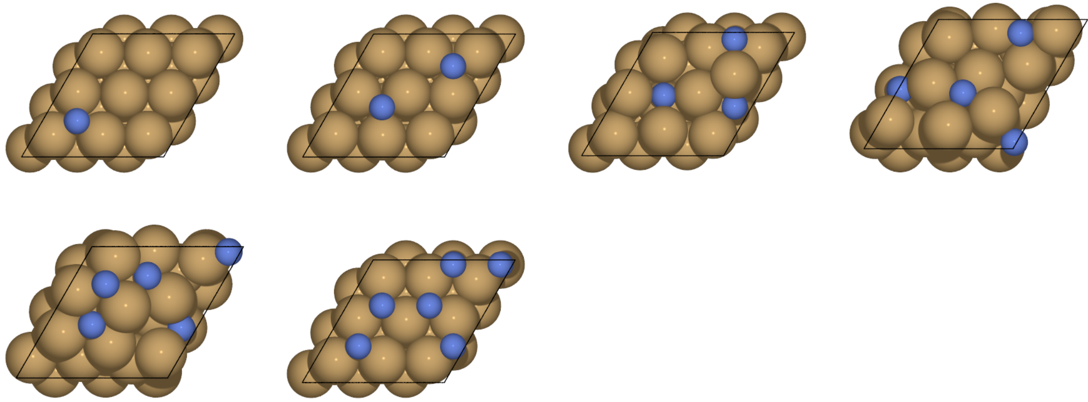

111

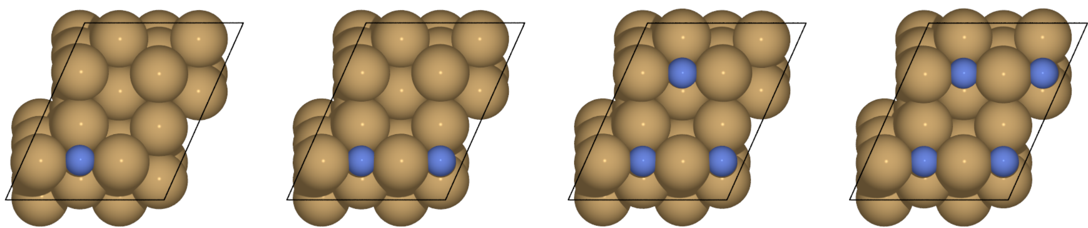

210

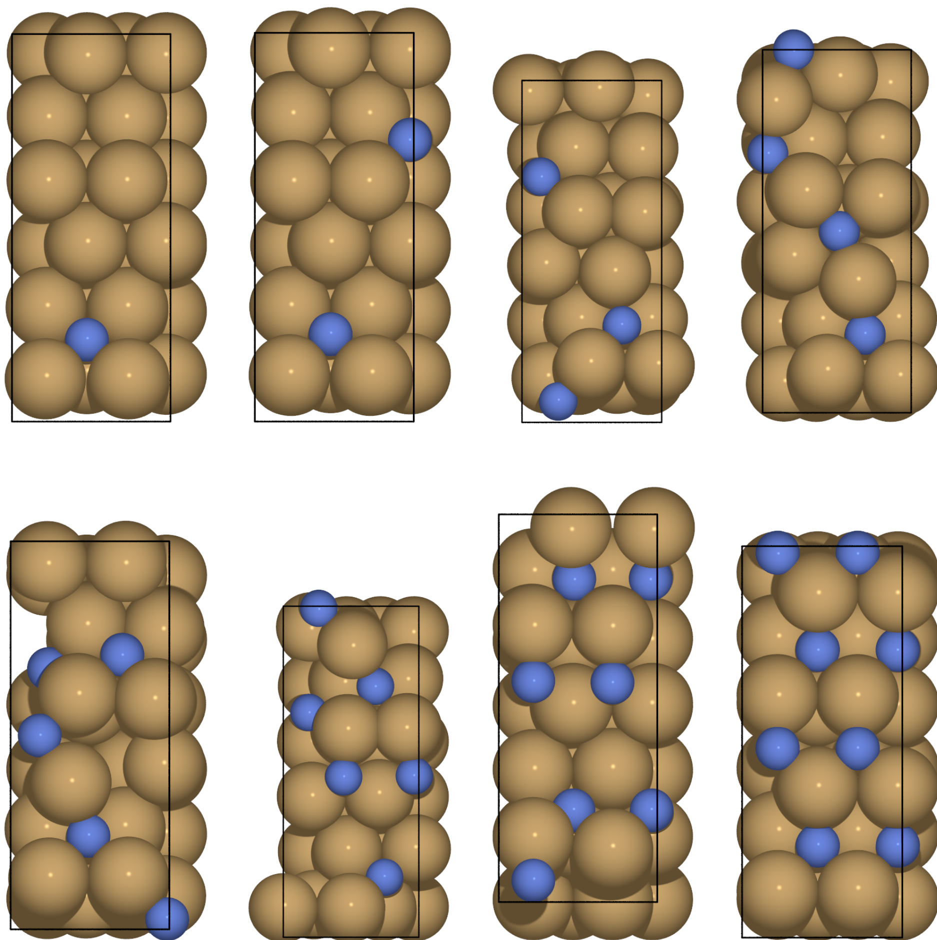

211

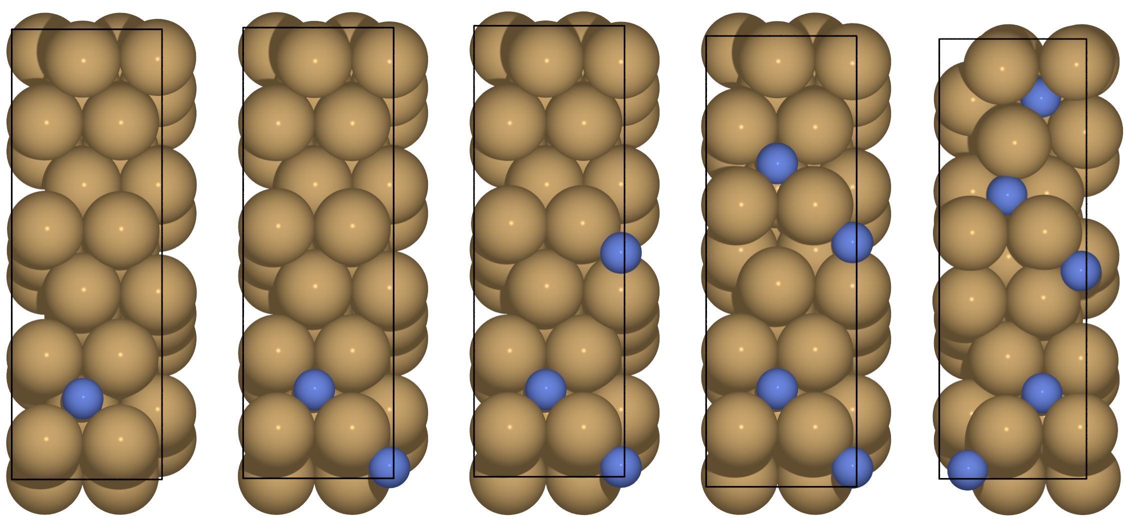

221

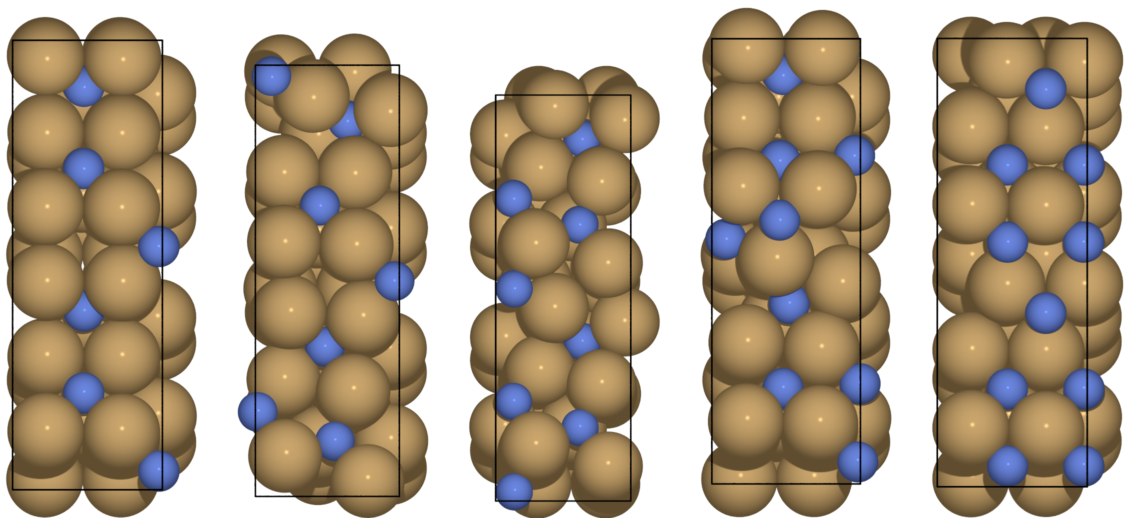

311

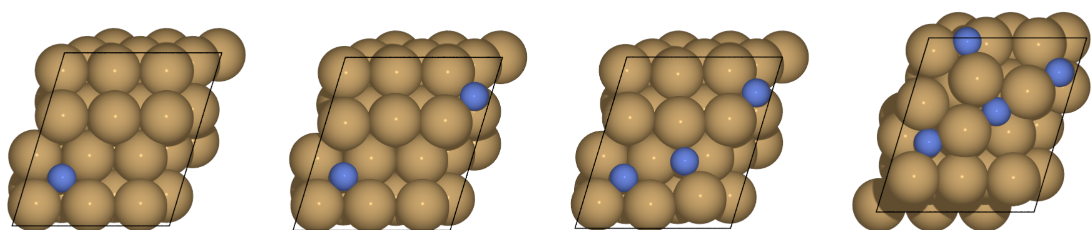

Figure C.2: Configuration search iterations for Cu/N system

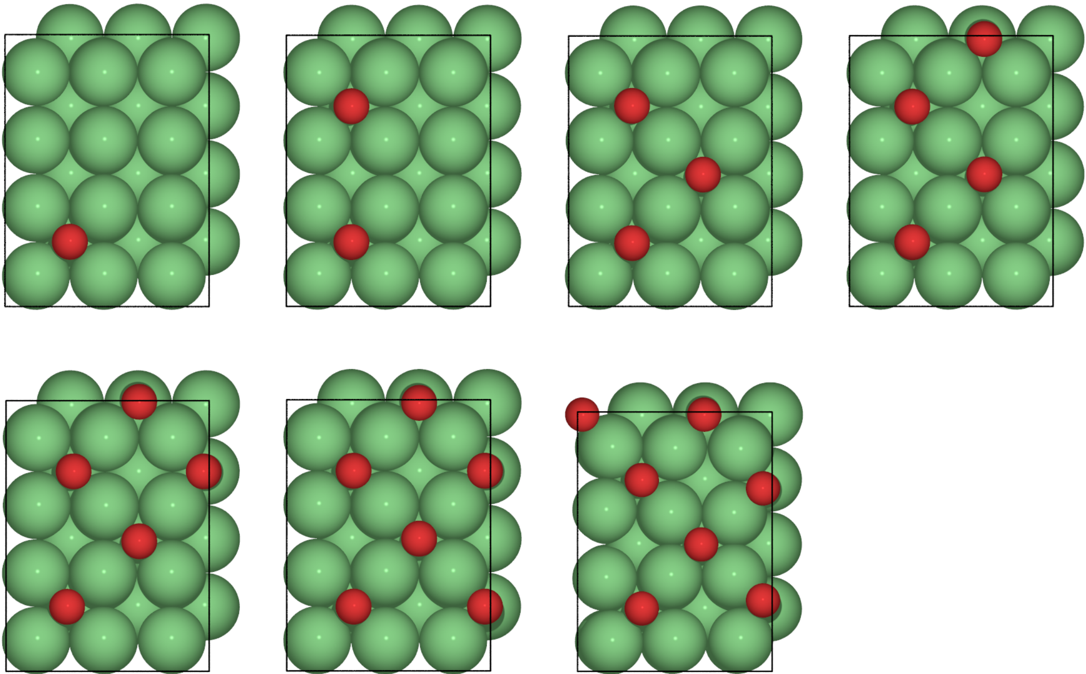
100

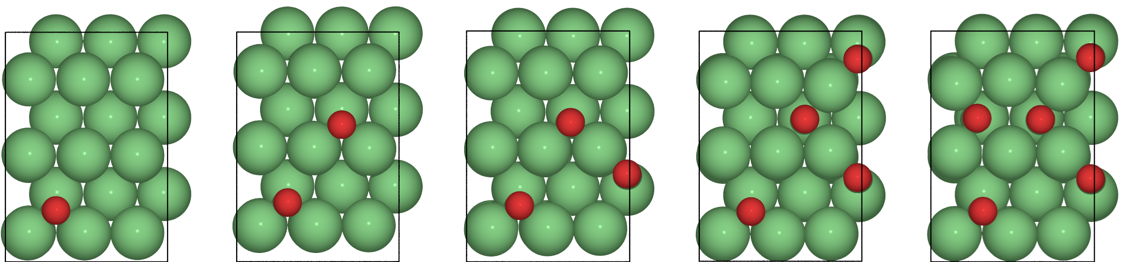
110

111

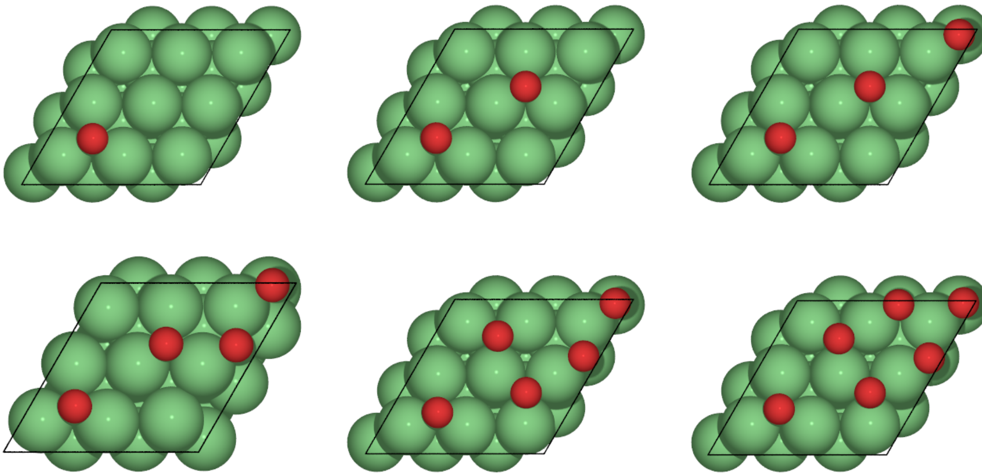

210

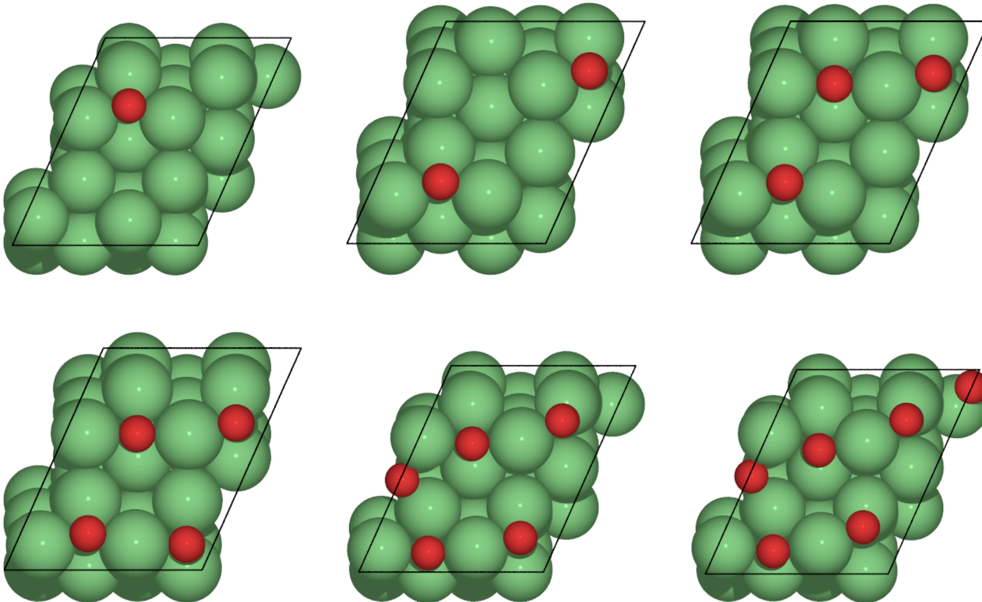

211

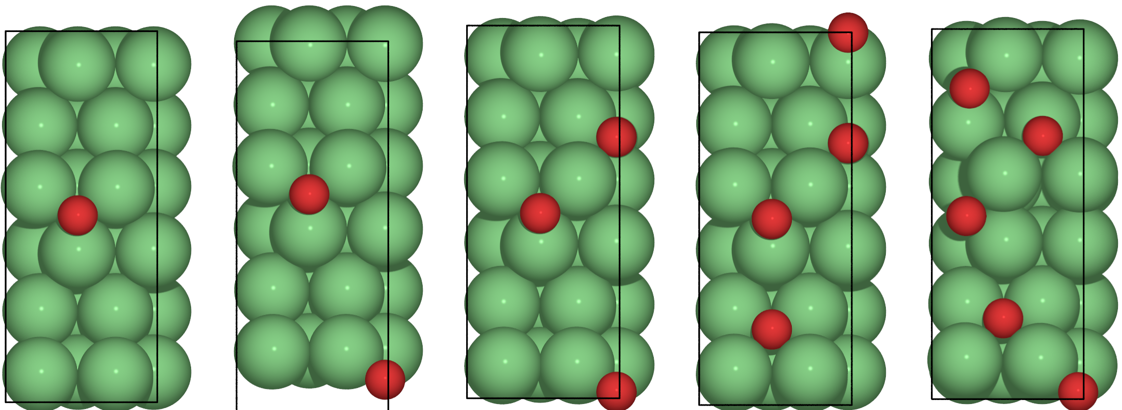

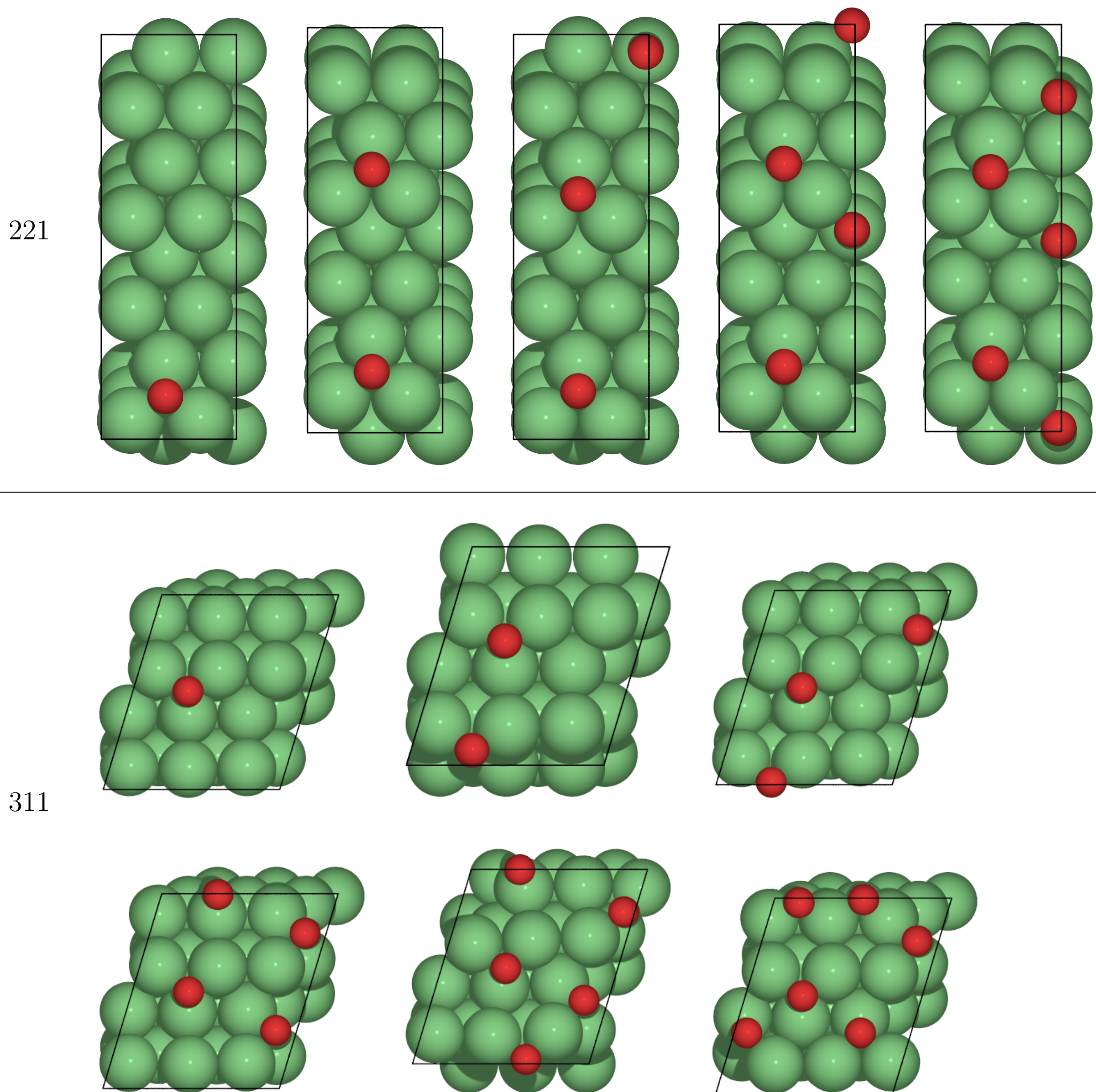

Figure C.3: Configuration search iterations for Ni/O system

100

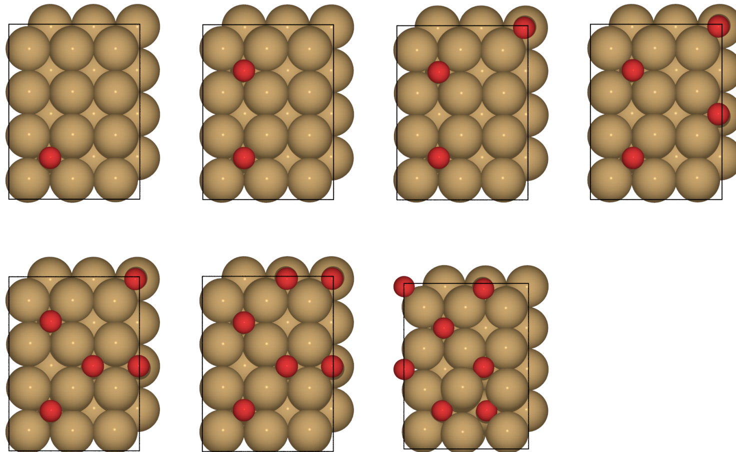

110

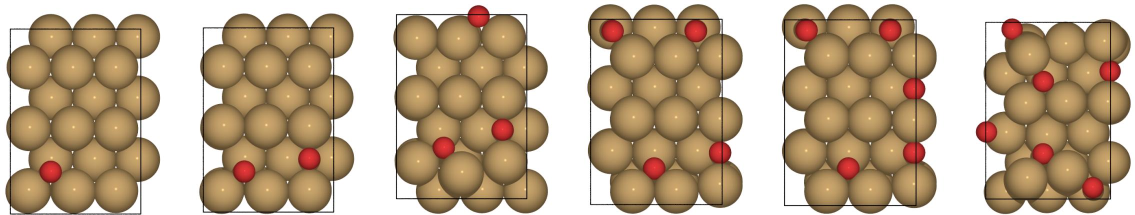

111

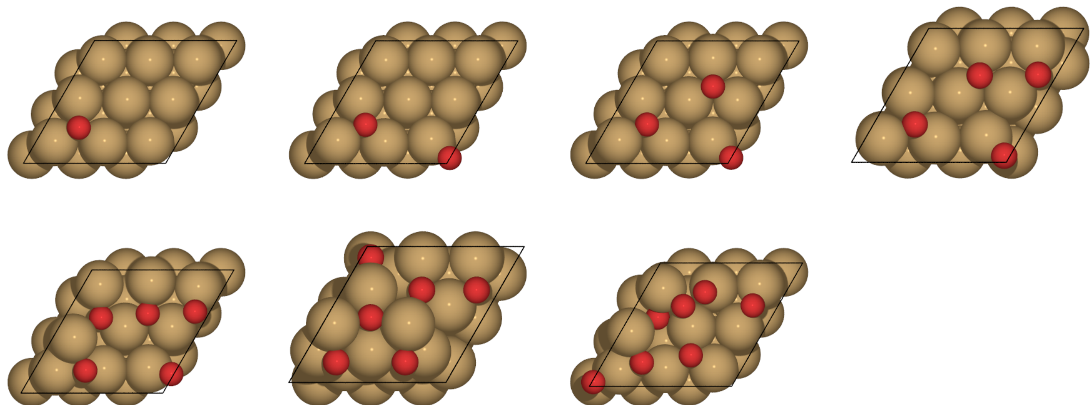

210

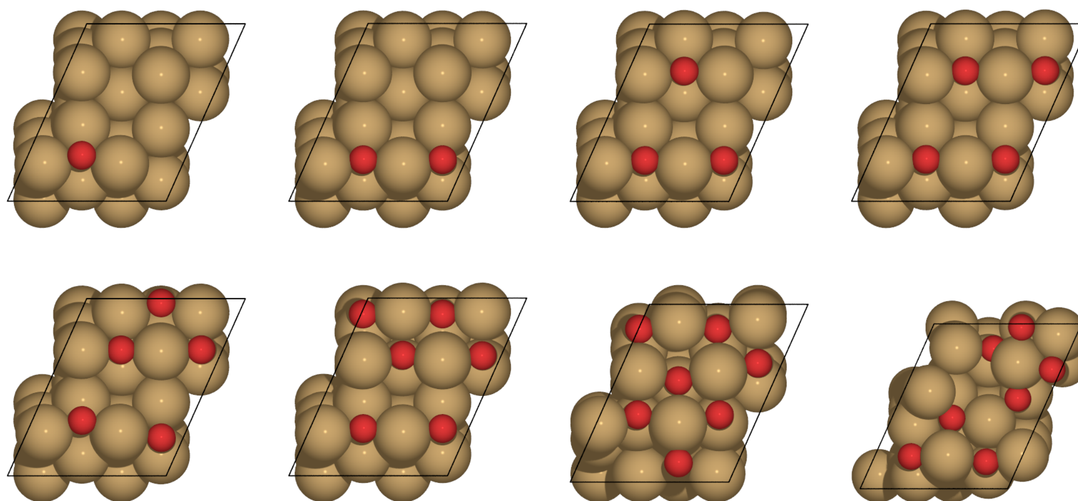

211

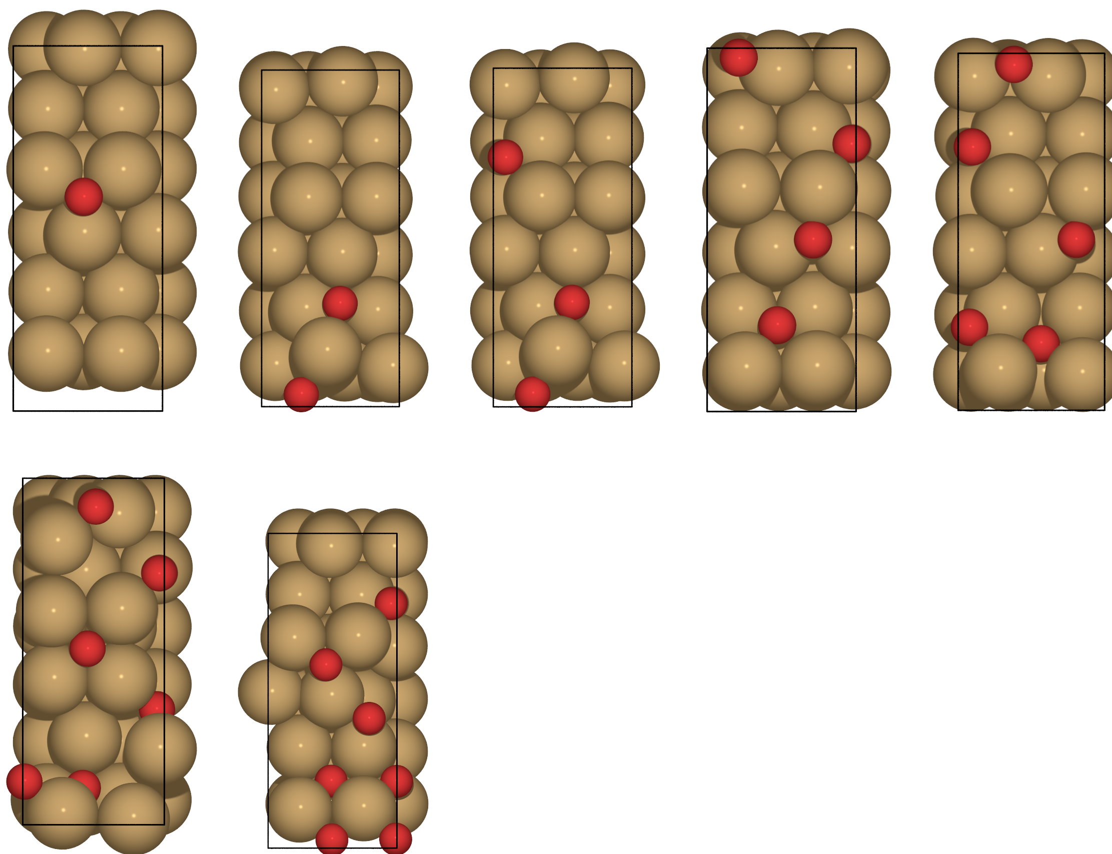

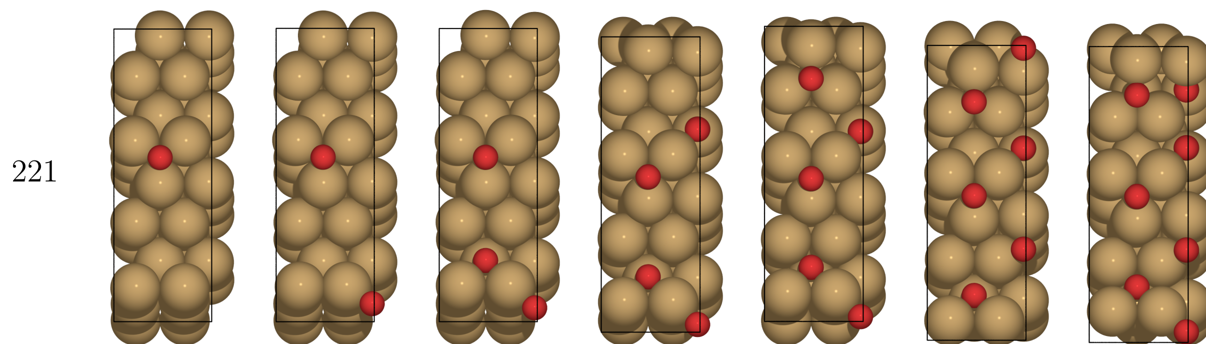

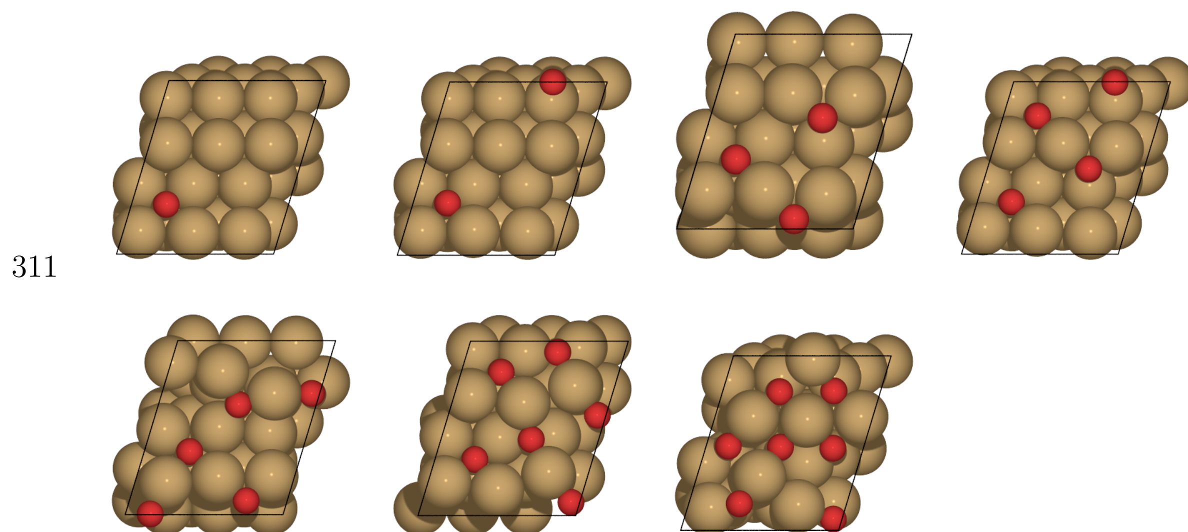

Figure C.4: Configuration search iterations for Cu/O system

Bibliography

[1] I Adamovich, S D Baalrud, A Bogaerts, P J Bruggeman, M Cappelli, V Colombo, U Czarnetzki, U Ebert, J G Eden, P Favia, D B Graves, S Hamaguchi, G Hieftje, M Hori, I D Kaganovich, U Kortshagen, M J Kushner, N J Mason, S Mazouffre, S Mededovic Thagard, H-R Metelmann, A Mizuno, E Moreau, A B Murphy, B A Niemira, G S Oehrlein, Z Lj Petrovic, L C Pitchford, Y-K Pu, S Rauf, O Sakai, S Samukawa, S Starikovskaia, J Tennyson, K Terashima, M M Turner, M C M van de Sanden, and A Vardelle. The 2017 plasma roadmap: Low temperature plasma science and technology. *Journal of Physics D: Applied Physics*, 50(32):323001, jul 2017.

[2] Satish D. Athavale and Demetre J. Economou. Molecular dynamics simulation of atomic layer etching of silicon. *Journal of Vacuum Science & Technology A*, 13(3):966–971, May 1995.

[3] P. Atkins and T. Overton. *Shriver and Atkins' Inorganic Chemistry*. OUP Oxford, 2010.

[4] A.M. Baró and L. Ollé. Adsorption site of oxygen chemisorption on ni(110) at room temperature; an eels study. *Surface Science*, 126(1):170 – 176, 1983.

[5] A. D. Becke. Density-functional exchange-energy approximation with correct asymptotic behavior. *Phys. Rev. A*, 38:3098–3100, Sep 1988.

[6] P. E. Blöchl. Projector augmented-wave method. *Phys. Rev. B*, 50:17953–17979, Dec 1994.

[7] B. J. Boyle, E. G. King, and K. C. Conway. Heats of formation of nickel and cobalt oxides (nio and coo) of combustion calorimetry. *Journal of the American Chemical Society*, 76(14):3835–3837, 1954.

[8] Colin T. Carver, John J. Plombon, Patricio E. Romero, Satyarth Suri, Tristan A. Tronic, and Robert B. Turkot. Atomic Layer Etching: An Industry Perspective. *ECS Journal of Solid State Science and Technology*, 4(6):N5005–N5009, January 2015.

[9] B. Chapman. *Glow Discharge Processes: Sputtering and Plasma Etching*. Wiley, 1980.

[10] F.F. Chen and J.P. Chang. *Lecture Notes on Principles of Plasma Processing*. Springer US, 2003.

[11] CRC Handbook. *CRC Handbook of Chemistry and Physics, 88th Edition*. CRC Press, 88 edition, 2007.

[12] X. Duan, O. Warschkow, A. Soon, B. Delley, and C. Stampfl. Density functional study of oxygen on cu(100) and cu(110) surfaces. *Phys. Rev. B*, 81:075430, Feb 2010.

[13] D.A. Edwards and R. Richards. The mass spectra of copper(i) carboxylates. *Inorganic and Nuclear Chemistry Letters*, 8(9):783 – 792, 1972.

[14] S. H. Elder, F. J. DiSalvo, L. Topor, and A. Navrotsky. Thermodynamics of ternary nitride formation by ammonolysis: application to lithium molybdenum nitride (limon2), sodium tungsten nitride (na3wn3), and sodium tungsten oxide nitride (na3wo3n). *Chemistry of Materials*, 5(10):1545–1553, 1993.

[15] Simon D. Elliott. Atomic-scale simulation of ALD chemistry. *Semiconductor Science and Technology*, 27(7):074008, June 2012.

[16] M. J. Frisch, G. W. Trucks, H. B. Schlegel, G. E. Scuseria, M. A. Robb, J. R. Cheeseman, G. Scalmani, V. Barone, G. A. Petersson, H. Nakatsuji, X. Li, M. Caricato, A. V. Marenich, J. Bloino, B. G. Janesko, R. Gomperts, B. Mennucci, H. P. Hratchian, J. V. Ortiz, A. F. Izmaylov, J. L. Sonnenberg, D. Williams-Young, F. Ding, F. Lipparini, F. Egidi, J. Goings, B. Peng, A. Petrone, T. Henderson, D. Ranasinghe, V. G. Zakrzewski, J. Gao, N. Rega, G. Zheng, W. Liang, M. Hada, M. Ehara, K. Toyota, R. Fukuda, J. Hasegawa, M. Ishida, T. Nakajima, Y. Honda, O. Kitao, H. Nakai, T. Vreven, K. Throssell, J. A. Montgomery, Jr., J. E. Peralta, F. Ogliaro, M. J. Bearpark, J. J. Heyd, E. N. Brothers, K. N. Kudin, V. N. Staroverov, T. A. Keith, R. Kobayashi, J. Normand, K. Raghavachari, A. P. Rendell, J. C. Burant, S. S. Iyengar, J. Tomasi, M. Cossi, J. M. Millam, M. Klene, C. Adamo, R. Cammi, J. W. Ochterski, R. L. Martin, K. Morokuma, O. Farkas, J. B. Foresman, and D. J. Fox. Gaussian˜16 Revision C.01, 2016. Gaussian Inc. Wallingford CT.

[17] D.W. Green and R.H. Perry. *Perry's Chemical Engineers' Handbook, Eighth Edition*. McGraw Hill professional. McGraw-Hill Education, 2007.

[18] N.N. Greenwood, N. Greenwood, A. Earnshaw, E. Earnshaw, and E. A. *Chemistry of the Elements*. Butterworth-Heinemann, 1984.

[19] P. Hohenberg and W. Kohn. Inhomogeneous electron gas. *Phys. Rev.*, 136:B864–B871, Nov 1964.

[20] Shona M. Johnston, Andrew Mulligan, Vin Dhanak, and Malcolm Kadodwala. The structure of disordered chemisorbed oxygen on cu(111). *Surface Science*, 519(1):57 – 63, 2002.

[21] Keren J. Kanarik, Thorsten Lill, Eric A. Hudson, Saravanapriyan Sriraman, Samantha Tan, Jeffrey Marks, Vahid Vahedi, and Richard A. Gottscho. Overview of atomic layer etching in the semiconductor industry. *Journal of Vacuum Science & Technology A*, 33(2):020802, 2015.

[22] Keren J. Kanarik, Samantha Tan, and Richard A. Gottscho. Atomic layer etching: Rethinking the art of etch. *The Journal of Physical Chemistry Letters*, 9(16):4814–4821, 2018. PMID: 30095919.

[23] W. Kohn and L. J. Sham. Self-consistent equations including exchange and correlation effects. *Phys. Rev.*, 140:A1133–A1138, Nov 1965.

[24] G. Kresse and J. Furthmüller. Efficient iterative schemes for ab initio total-energy calculations using a plane-wave basis set. *Phys. Rev. B*, 54:11169–11186, Oct 1996.

[25] G. Kresse and J. Furthmüller. Efficiency of ab-initio total energy calculations for metals and semiconductors using a plane-wave basis set. *Computational Materials Science*, 6(1):15 – 50, 1996.

[26] G. Kresse and D. Joubert. From ultrasoft pseudopotentials to the projector augmented-wave method. *Phys. Rev. B*, 59:1758–1775, Jan 1999.

[27] Chengteh Lee, Weitao Yang, and Robert G. Parr. Development of the colle-salvetti correlation-energy formula into a functional of the electron density. *Phys. Rev. B*, 37:785–789, Jan 1988.

[28] Jiaye Li, Jinping Wu, Chenggang Zhou, Bo Han, Xinjian Lei, Roy Gordon, and Hansong Cheng. On the relative stability of cobalt- and nickel-based amidinate complexes against Î²-migration. *International Journal of Quantum Chemistry*, 109(4):756–763, March 2009.

[29] Z. Li and R.G. Gordon. Thin, continuous, and conformal copper films by reduction of atomic layer deposited copper nitride. *Chemical Vapor Deposition*, 12(7):435–441, 2006.

[30] Zhefeng Li, Roy G. Gordon, Venkateswara Pallem, Huazhi Li, and Deo V. Shenai. Direct-Liquid-Injection Chemical Vapor Deposition of Nickel Nitride Films and Their Reduction to Nickel Films. *Chemistry of Materials*, 22(10):3060–3066, May 2010.

[31] Zhengwen Li, SeÃ¡n T. Barry, and Roy G. Gordon. Synthesis and Characterization of Copper(I) Amidinates as Precursors for Atomic Layer Deposition (ALD) of Copper Metal. *Inorganic Chemistry*, 44(6):1728–1735, March 2005.

[32] Booyong S. Lim, Antti Rahtu, and Roy G. Gordon. Atomic layer deposition of transition metals. *Nature Materials*, 2(11):749–754, November 2003.

[33] Jianyi Lin, Koon Gee Neoh, and Wah koon Teo. Thermogravimetry–ftir study of the surface formate decomposition on cu, cucl, cu2o and cuo. correlations between reaction selectivity and structural properties. *J. Chem. Soc., Faraday Trans.*, 90:355–362, 1994.

[34] S. López-Moreno and A. H. Romero. Atomic and molecular oxygen adsorbed on (111) transition metal surfaces: Cu and ni. *The Journal of Chemical Physics*, 142(15):154702, 2015.

[35] Elham Mohimi, Xiaoqing I. Chu, Brian B. Trinh, Shaista Babar, Gregory S. Girolami, and John R. Abelson. Thermal Atomic Layer Etching of Copper by Sequential Steps Involving Oxidation and Exposure to Hexafluoroacetylacetone. *ECS Journal of Solid State Science and Technology*, 7(9):P491–P495, January 2018.

[36] T. Narusawa, W.M. Gibson, and E. Törnqvist. Structure study of oxygen-adsorbed ni(111) surface by high energy ion scattering. *Surface Science*, 114(1):331 – 348, 1982.

[37] Christian A. Nijhuis, Erica Jellema, Timo J. J. Sciarone, Auke Meetsma, Peter H. M. Budzelaar, and Bart Hessen. First-Row Transition Metal Bis(amidinate) Complexes; Planar Four-Coordination of FeII Enforced by Sterically Demanding Aryl Substituents. *European Journal of Inorganic Chemistry*, 2005(11):2089–2099, June 2005.

[38] Toshikazu Nosaka, Masaaki Yoshitake, Akio Okamoto, Soichi Ogawa, and Yoshikazu Nakayama. Copper nitride thin films prepared by reactive radio-frequency magnetron sputtering. *Thin Solid Films*, 348(1):8 – 13, 1999.

[39] Tetsuya Ogura and Quintus Fernando. Mass spectrometry and structures of copper(i) carboxylates in the vapor phase. *Inorganic Chemistry*, 12(11):2611–2615, 1973.

[40] Tetsuya. Ogura, Richard D. Mounts, and Quintus. Fernando. Structure of a planar four-coordinate complex of copper(i). *Journal of the American Chemical Society*, 95(3):949–951, 1973.

[41] Jae-Min Park, Kwangseon Jin, Byeol Han, Myung Jun Kim, Jongwan Jung, Jae Jeong Kim, and Won-Jun Lee. Atomic layer deposition of copper nitride film and its application to copper seed layer for electrodeposition. *Thin Solid Films*, 556:434 – 439, 2014.

[42] John P. Perdew, Kieron Burke, and Matthias Ernzerhof. Generalized gradient approximation made simple. *Phys. Rev. Lett.*, 77:3865–3868, Oct 1996.

[43] J. M. Rahm and P. Erhart. Wulffpack: A python package for wulff constructions. *J. Open Source Softw.*, 5:1944, 2020.

[44] S. Rauf, T. Sparks, P. L. G. Ventzek, V. V. Smirnov, A. V. Stengach, K. G. Gaynullin, and V. A. Pavlovsky. A molecular dynamics investigation of fluorocarbon based layer-by-layer etching of silicon and SiO2. *Journal of Applied Physics*, 101(3):033308, February 2007.

[45] Xia Sang, Yantao Xia, Philippe Sautet, and Jane P. Chang. Atomic layer etching of metals with anisotropy, specificity, and selectivity. *Journal of Vacuum Science and Technology A*, Forthcoming, 2020.

[46] Aloysius Soon, Mira Todorova, Bernard Delley, and Catherine Stampfl. Oxygen adsorption and stability of surface oxides on Cu(111): A first-principles investigation. *Phys. Rev. B*, 73:165424, Apr 2006.

[47] Samantha Tan, Wenbing Yang, Keren J. Kanarik, Thorsten Lill, Vahid Vahedi, Jeff Marks, and Richard A. Gottscho. Highly selective directional atomic layer etching of silicon. *ECS Journal of Solid State Science and Technology*, 4(6):N5010–N5012, 2015.

[48] D. Vempaire, S. Miraglia, A. Sulpice, L. Ortega, E.K. Hlil, D. Fruchart, and J. Pelletier. Structure and magnetic properties of nickel nitride thin film synthesized by plasma-based ion implantation. *Journal of Magnetism and Magnetic Materials*, 272-276(6):E843–E844, 2004. Place: Netherlands.

[49] D. Vempaire, S. Miraglia, A. Sulpice, L. Ortega, E.K. Hlil, D. Fruchart, and J. Pelletier. Structure and magnetic properties of nickel nitride thin film synthesized by plasma-based ion implantation. *Journal of Magnetism and Magnetic Materials*, 272-276:E843 – E844, 2004. Proceedings of the International Conference on Magnetism (ICM 2003).

[50] Katja Väyrynen, Timo Hatanpää, Miika Mattinen, Mikko J. Heikkilä, Kenichiro Mizohata, Jyrki Räisänen, Joosep Link, Raivo Stern, Mikko Ritala, and Markku Leskelä. Atomic layer deposition of nickel nitride thin films using nicl2(tmpda) and tert-butylhydrazine as precursors. *physica status solidi (a)*, 216(11):1900058, 2019.

[51] Tao Wang, Zhen Yan, Carine Michel, Marc Pera-Titus, and Philippe Sautet. Trends and Control in the Nitridation of Transition-Metal Surfaces. *ACS Catalysis*, 8(1):63–68, January 2018.

[52] Kazutoshi Yagi-Watanabe, Yoshiko Ikeda, Yasuhiro Ishii, Tamami Inokuchi, and Hirohito Fukutani. Reaction kinetics and mechanism of oxygen adsorption on the ni(110) surface. *Surface Science*, 482-485:128 – 133, 2001.

[53] Kazuko Zenmyo, Hidenori Kubo, Masahiko Tokita, and Kazuo Yamagata. Proton nmr study of nickel formate di-hydrate, ni(hcoo)2Â·2h2o. *Journal of the Physical Society of Japan*, 75(10):104704, 2006.

[54] Guangan Zhang, Zhibin Lu, Jibin Pu, Guizhi Wu, and Kaiyuan Wang. Structure and Thermal Stability of Copper Nitride Thin Films. *Indian Journal of Materials Science*, 2013:725975, December 2013. Publisher: Hindawi Publishing Corporation.